Open-Switch Fault Diagnosis in Back-to-Back NPC Converters of PMSG-Based WTS via Zero Range Value of Phase Currents

Ganesh Mayilsamy, Seong Ryong Lee, and Young Hoon Joo

***Abstract*—This study aims to enhance the reliability and availability of a three-level neutral point clamped (NPC) converter of a permanent magnet synchronous generator (PMSG)-based high-power wind turbine system by proposing a multiple open-switch (OS) fault diagnosis method. The OS faults lead to severe torque pulsation and distorted grid current in the system, hence requiring early detection and isolation. To do this, principal diagnostic variables are first formulated using the zero range value of instantaneous current amplitude and dc-link capacitor voltages. Then, the diagnostic variables detect the state of power electronic switches of each leg of the converters without being affected by torque pulsations, speed variations, and system power factor. Second, a fault localization scheme is introduced with identification thresholds to indicate the faulty switches of the machine side converter (MSC) and grid side converter (GSC). In GSC fault identification, an equivalent current transformation is employed to avoid errors in current normalization. Finally, the effectiveness of the proposed method is confirmed by verifying the results of comparative studies, simulations, hardware experimentation, and robustness against false indications in MSC and GSC.**

***Index Terms*—Multiple open-switch (OS) faults, neutral point clamped (NPC) converter, permanent magnet synchronous generator (PMSG), wind turbine system (WTS).**

I. Introduction

HIGH power-rated permanent magnet synchronous generators (PMSGs) are finding widespread applications in multi-MW wind turbine systems (WTSs) because of their attractive nature of direct-drive capability, increased reliability, higher efficiency, and improved power density [1], [2]. Similarly, the converter selection becomes essential to support high-power grid-connected WTSs. Therefore, the three-level (3 L) back-to-back (BTB) NPC, medium-voltage converter constructed with integrated gate commutated-thyristor (IGCT) is found to be the promising configuration for the grid-connected operation of 10-MW rated high-power WTS with PMSGs [3]. Moreover, the NPC BTB configuration presents higher voltage levels, low harmonic distortion, and improved power conversion efficiency [4]. Furthermore, there has been considerable research to justify the use of NPC converters in high-power WTSs [5], [6], [7]. Since the NPC BTB converter topology is composed of many semiconductor switching devices, the possibility of device fault increases with variable speed drives, this is a recent concern among many of the research [8].

The converter failure in a WTS is attributable to 14.3% of the total annual downtime [9]. Regarding the statistical analysis of power converter equipment failure in WTSs, it is indicated that 35% of converter failure is due to semiconductor switch fault and the printed circuit board, connectors, and joint failure account, respectively, for 32%, 4%, and 19% of converter failure. The remaining 10% of faults are due to other reasons [10]. An industry-based survey on the reliability of power electronic systems has pointed out that the gate driver failure and semiconductor switch failure account for 15% and 31%, respectively, for the converter outages. In addition, the survey on dc–dc power converter systems has revealed that a major chunk of converter failure rate is attributed to semiconductor devices (57%) or their gate drivers (19%) [11]. Therefore, it can be concluded that a considerable percentage of converter failures are due to semiconductor switch faults and gate driver failures.

Besides, the device failure may result from the destructive over-current due to a short-circuit fault, which is of serious concern, hence required to be detected and isolated within 10μs [12]. Moreover, the heavy inrush current makes the formulation of integrated fault detection easier. Therefore, current limit-based hardware protection can be integrated as a standard design into the gate drivers of IGCTs [13], [14], [15]. On the other hand, the OS fault resulting from bond wire liftoff or gate driver failure does not result in severe concern and has no standard integrated protection design as its effect varies for different converter topologies. Despite this, the distortion in current and voltage caused by the OS fault leads to torque pulsation in PMSG, which also affects the grid power factor. Consequently, it results in the failure of other devices in the WTS structure, resulting in an entire shut-down [16]. Therefore, OS fault detection and diagnosis are essential to improve the reliability and availability

Manuscript received 16 June 2023; revised 25 September 2023 and 16 November 2023; accepted 23 December 2023. Date of publication 27 December 2023; date of current version 16 February 2024. This work was supported in part by the Basic Science Research Program under Grants NRF-2016R1A6A1A03013567 and NRF-2018R1A2A2A14023632, in part by the framework of International Cooperation Program under Grant NRF-2022 K2A9A2A06045121 through the National Research Foundation of Korea (NRF) funded by the Ministry of Education. Recommended for publication by Associate Editor T. Shi. *(Corresponding author: Young Hoon Joo.)*

The authors are with the Research Center for Wind Energy Systems, Kunsan National University, Gunsan 573-701, South Korea (e-mail: ganesh@kunsan.ac.kr; srlee@kunsan.ac.kr; yhjoo@kunsan.ac.kr).

Color versions of one or more figures in this article are available at https://doi.org/10.1109/TPEL.2023.3347563.

Digital Object Identifier 10.1109/TPEL.2023.3347563

of WTSs. In this regard, there is numerous research on effective OS fault detection and identification procedures. A great deal of pole voltage-based methods are presented for reliable and fast diagnosis [17], [18]. Nevertheless, these methods require additional sensors and circuits, adding up the control system's complexity. Few recent research has addressed this by voltage quantification and estimation [8], [19], [20], but still, it requires higher sampling and increased complexity. Moreover, all these methods are tested with constant dc-source; hence, the adaptability to WTSs with varying rotor speeds has not been verified.

Meanwhile, the current-based schemes have garnered some attraction for OS fault diagnosis in BTB converters. Moreover, these methods are free from model dependency, simple to implement, and do not need any additional sensors. A diagnostic approach for a two-level (2 L) BTB converter of WTS based on averaging the phase current is introduced in [21], in which the derivative of Park's vector angle and the average value of current are the primary variable for detection and localization. In [22], a Luenberger current observer and current farm factors are used as the primary variables. These methods are found to be reliable and less sensitive to load disturbances but require at least one fundamental period of current to detect the fault. An instantaneous amplitude estimation based on weighted sliding Hilbert transform is presented in [23] to overcome this. In which, detection speed has been considerably improved with less model dependency. Although all these methods are only tested and verified with a 2 L BTB converter for WTS operation.

In addition, virtual current mirrors are justified as an effective variable for 2 L voltage source inverter (VSI) fault identification [24]. Any extension of this scheme to three-level (3 L) BTB converters may be possible for inner-switch ($S^x_{y_2}$, $S^x_{y_3}$) faults, which have an identical current response to 2 L BTB converters. Besides, the outer-switch ($S^x_{y_1}$, $S^x_{y_4}$) faults exhibit divergent behavior based on many factors, such as power factor, rectification, and inverter mode of operations. It further complicates the adaptation of these methods to 3 L converters. Therefore, to deal with the distinct current patterns of outer and inner switches, a reactive power injection-based method [25] is introduced. Alongside, the model-based schemes, which use the voltage residuals between the monitored and estimated signals, are studied in [8], [19], [26], [27], [28]. The appropriateness of these methods is confirmed only to the grid-connected VSI.

Moreover in WTSs, the rectification operation provides additional current paths through the freewheeling diodes and differs from the inverter operation. Thus, the ideas cannot be applied simultaneously to both GSC and MSC. To subdue this, the current distortions caused by different switch faults in the BTB NPC converter of a WTS are analyzed, and the fault localization method is formulated based on the zero range duration of currents [29]. With this, better localization of faulty switches can be achieved for nonunity power factor (NUPF) operation with a trade-off in detection time. However, the unity power factor (UPF) operation does not differentiate the inner and outer-switch faults. Since the GSC of WTS has to operate in UPF most of the time, this is a significant discrepancy.

Moreover, the signal attributes of inner and outer-switch faults are indistinguishable, especially under UPF. In addition, imperceptible outer-switch faults occur in GSC [20]. This issue still needs to be addressed in NPC BTB fault localization of WTSs regarding high-power rating. Therefore, this article aims to propose a new OS fault diagnosis with the contributions summarized as follows:

1) A zero range variable (ZRV) is defined to identify the current ripple during zero crossing under OS faults. Then, the detection and diagnosis variable γ is formulated by analyzing the frequency of ripples in ZRV.
2) Next, an improved current-based scheme is formulated as Algorithms 1, and 2, respectively for MSC and GSC to detect and localize the faulty switch by utilizing the range of γ values.
3) An equivalent current transformation from the machine side to the grid side for the active power component is introduced using the WTS rotor speed. Which avoids the errors in current normalization.
4) The proposed method is validated by simulation for 10 MW PMSG-based WTS. Further, the applicability and robustness of the proposed algorithms are verified by hardware implementation for 5 kW permanent magnet vernier generator (PMVG)-based WTSs.
5) The performance of the presented ZRV-based scheme is compared with the other relevant current-based schemes for various performance indicators.

The rest of this article is organized as follows. Section II analyses the BTB NPC converter signal attributes of PMSG-based high-power WTS under different OS faults. Section III discusses the formulation of OS fault diagnosis algorithms for MSC and GSC. Section IV presents the simulation results and hardware implementation to signify the constructiveness and robustness of the proposed method. Finally, Section V concludes this article.

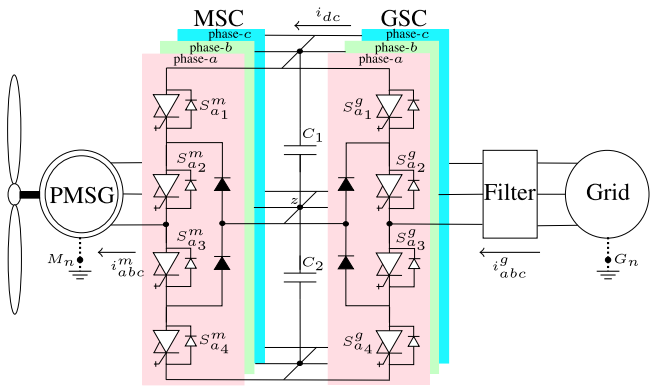

Fig. 1. High-power WTS structure with back-to-back NPC converters.

II. System Description and OS Fault Analysis

The general structure of high-power rated PMSG-based WTS with 3 L NPC converter is shown in Fig. 1. The power conversion system comprises a wind turbine, PMSG, BTB converter with NPC converter topology, and a grid-connected inductive filter. The BTB topology comprises MSC, and GSC interlinked by two dc-link capacitors. The converters are typically configured

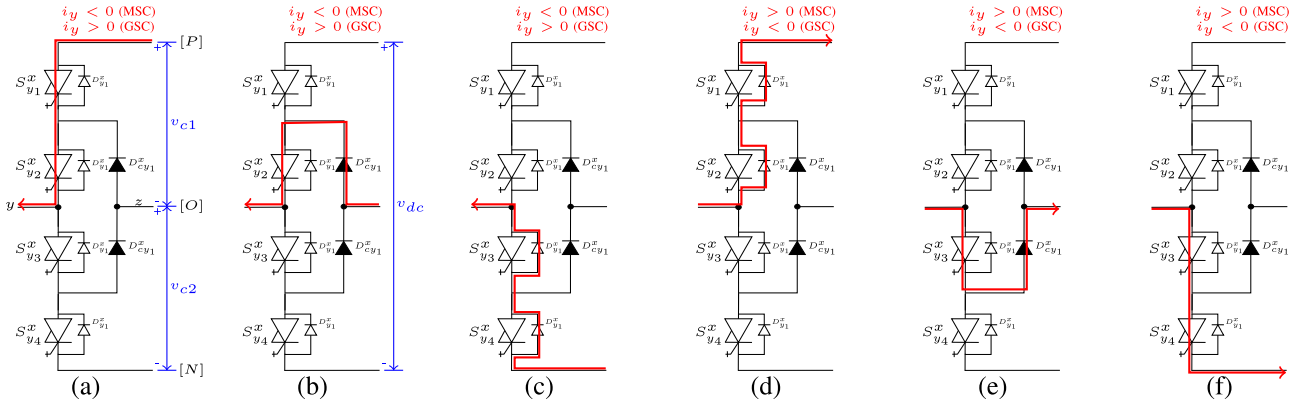

Fig. 2. Current paths of rectification/inverter operation for current direction from dc-link to phase-y with switching states (a) $[P]$, (b) $[O]$, and (c) $[N]$. Current paths of rectification/inverter operation for current direction from phase-y to DC-link with switching states (d) $[P]$, (e) $[O]$, and (f) $[N]$.

with IGCT switches with antiparallel power diodes to withstand the higher amplitude of operating current and voltages. The GSC control system ensures the dc-link voltage regulation, capacitor voltage balancing, and reactive power injection. On the other hand, the MSC takes control of the PMSG operating speed (ω_m)-based on the tracking signal from maximum power extraction unit [7], [30]. The current and voltage sensors measure the machine, grid, and dc-link parameters. Each leg of the GSC and MSC consists of four switches, S^x_{y1}, S^x_{y2}, S^x_{y3}, and S^x_{y4}, where $x \in (m, g)$ denote the machine, grid and $y \in (a, b, c)$ denote the phases. Fig. 2 illustrates the current paths based on the direction of current between any phase-y and the dc-link with three possible switching states $[P], [O], [N]$ under MSC rectification and GSC inverter operations. An OS fault in any switch will distort the respective BTB converter current and affect the dc-link capacitor voltages. For understanding, the OS fault of different phase-a leg switches is considered for the MSC and GSC, respectively, in the following discussions. The details regarding the switching states and current directions are referred from [29].

A. Signal Attributes of MSC With Various OS Faults

The MSC operating parameters with normal and faulty switch conditions under steady load on PMSG (constant wind velocity) are shown in Figs. 3–5. The fault in switch S^m_{a1} does not allow the switching state $[P]$ to be realized; however, switching state $[O]$ is possible, hence, the current path for $i_y < 0$ changes from Fig. 2(a) to (b). Consequently, the pole voltage v^m_{az} changes from v_{c1} to 0 (switching state $[P]$ to $[O]$). As a result, the OS fault causes a distorted negative current and the pole voltage of phase-a is also distorted in the blocked interval, which is depicted in Fig. 3(a). However, the positive portion remains sinusoidal in shape due to the unaffected current path $i_y > 0$ in Fig. 2(d) and (e). Further, the occurrence of fault causes the phase current i^m_a to remain in zero for a shorter duration after zero crossing from the positive side and also affects the pattern of i^m_b and i^m_c as pictured in Fig. 3(b). On the other hand, the OS fault in S^m_{a4} blocks the switching state $[N]$ and blocks the current path shown in Fig. 2(e), which originates the opposite effect to

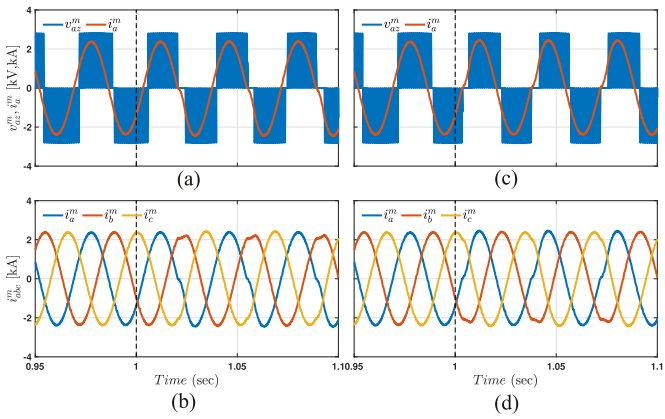

Fig. 3. MSC signal attributes: (a) and (b) Pole voltage and currents under S^m_{a1} fault; (c) and (d) Pole voltage and currents under S^m_{a4} fault.

S^m_{a1} fault as given in the Fig. 3(c) and (d). The blocked states $[P]$ and $[N]$, respectively, for fault in S^m_{a1} and S^m_{a4}, have little impact in capacitor voltages, as drawn in Fig. 5(a). However, the current distortions initiated by the fault slightly affect the sine wave pattern of phase currents. As a result, the electromagnetic torque developed in the PMSG becomes distorted and creates a considerable rotor speed and torque pulsations, which are depicted in Fig. 5(b) and (c).

Next, the fault in S^m_{a2} prevents the switching states $[P], [N]$ by blocking the current path in Fig. 2(a), (b) for the current $i_y < 0$. This makes the inner circuit of MSC to be open-circuited, therefore the current path of phase-a switches to the path in Fig. 2(c) to the switching state $[N]$. Consequently, the pole voltage v^m_{az} changes from 0 to $-v_{c2}$ resulting in a serious distortion in phase-a current remaining in zero value for a longer duration at the negative half cycle. Similarly, the S^m_{a2} fault blocks the current paths in Fig. 2(e), (f) and switches to Fig. 2(d) by allowing only the switching state $[P]$. For this, the positive half cycle of phase-a current will be distorted by remaining in zero for a longer duration. Further, the application of switching state N for the S^m_{a2} fault makes the $-v_{c2}$ remain connected to the phase-a for the entire negative current duration $i_y < 0$. This

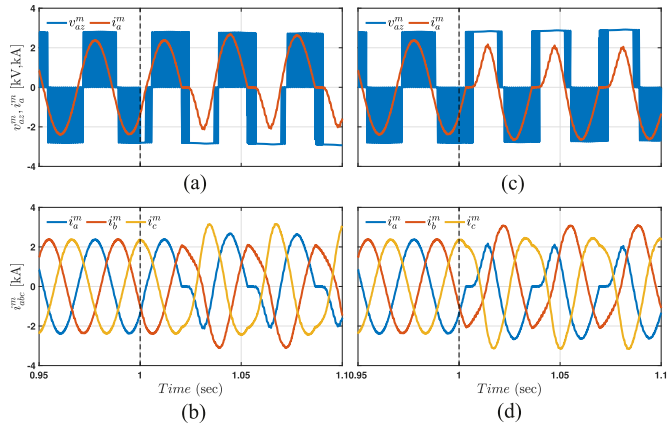

Fig. 4. MSC signal attributes: (a) and (b) Pole voltage and currents under $S^m_{a_2}$ fault; (c) and (d) Pole voltage and currents under $S^m_{a_3}$ fault.

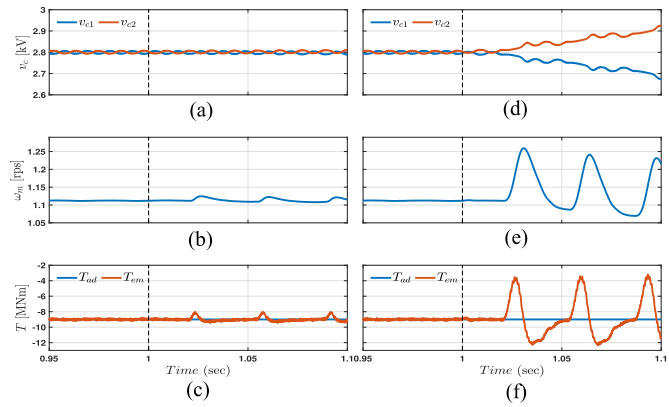

Fig. 5. MSC signal responses: (a) Capacitor voltages, (b) rotor speed, (c) torque responses with outer-switch fault; (d) capacitor voltages, (e) rotor speed, (f) torque responses with inner-switch fault.

causes the capacitor voltage v_{c2} to become larger than the v_{c1} leading to a dc-link imbalance. Similarly, the $S^m_{a_3}$ fault increase the v_{c1} and causes dc-link imbalance.

The MSC parameters under OS fault in $S^m_{a_2}$ and $S^m_{a_3}$ are given in Fig. 4. The current and pole voltage phase differs by some angle due to the NUPF of PMSG. The rectifier operation of MSC provides a freewheeling path through the diodes to carry the part of the positive and negative half cycle of current. Hence, the current remains zero for a duration only until the switching state $[O]$ is blocked due to the OS fault in $S^m_{a_2}$ and $S^m_{a_3}$, respectively, for the positive and negative half cycle. At the same time, the blocked switching states impact the pole voltages; the response of phase-a pole voltage and current is given for $S^m_{a_2}$ and $S^m_{a_3}$ faults in Fig. 4(a) and (c). Further, the distortion in i^m_a causes an unbalance in i^m_b and i^m_c as pictured in Fig. 4(b) and (d), respectively. The distortion caused by the inner switch fault in phase currents is comparatively higher than the outer switch fault, therefore resulting in more pulsation in the electromagnetic torque of PMSG. The effect of $S^m_{a_2}$ OS faults in capacitor voltages, speed, and torque of the PMSG is depicted in Fig. 5(d)–(f). Besides, an opposite effect in capacitor voltages will be experienced for the $S^m_{a_3}$ OS fault causing similar disturbances in speed and torque.

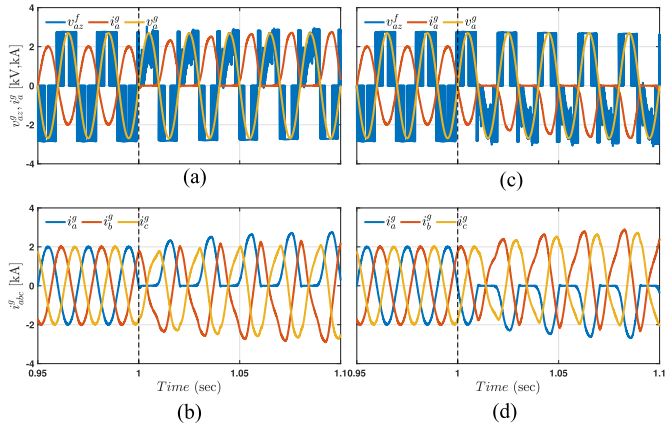

Fig. 6. GSC signal attributes under UPF: (a) and (b) Pole voltage and currents during $S^g_{a_1}$, $S^g_{a_2}$ fault; (c) and (d) Pole voltage and currents during $S^g_{a_3}$ and $S^g_{a_4}$ faults.

B. Signal Attributes of GSC With Various OS Faults

The effect of OS fault in the switches $S^g_{a_1}$, $S^g_{a_2}$, $S^g_{a_3}$, and $S^g_{a_4}$ under UPF operation are detailed in [25]. Unlike the MSC rectification operation, the GSC operates as a grid-connected inverter and most of the current flows through the IGCT switches. Regarding phase-a, the switches $S^g_{a_1}$, $S^g_{a_2}$ forms the path for $i_y > 0$ with switching state $[P]$ as shown in Fig. 2(a) and the switching sate $[N]$ is realized as in Fig. 2(b). Therefore, for the OS fault in switch $S^g_{a_1}$, the switching state $[P]$ is not possible, however, switching state $[O]$ is functionally possible. The occurrence of fault with $i_y > 0$ changes the current path from Fig. 2(a) to (b) until the current decays to zero. After that, the diode $D^g_{ca_1}$ is reverse biased due to the positive grid voltage. As a result, there are no current paths and the current $i_y > 0$ does not flow to the grid. At this time, the v_{c1} becomes larger than the v_{c2} and causes severe capacitor voltage imbalance. Alternately, for the fault in switch $S^g_{a_2}$ during the current $i_y > 0$, both current paths in Fig. 2(a) and (b) will not be available, respectively, for the switching states $[P], [N]$. At this time, the current takes its path as in Fig. 2(c) for a while until the current reaches zero value. Subsequently, the diodes are reverse-biased and no more paths will be available for the current flow from the dc-link to the grid. Moreover, the faults in switches $S^g_{a_1}$, $S^g_{a_2}$ create identical effect in the operation of GSC. Similarly, the OS fault in $S^g_{a_3}$ and $S^g_{a_4}$ affects the current paths in Fig. 2(f) and blocks the switching states $[O], [N]$. Consequently, the current $i_y < 0$ is blocked with v_{c2} increasing above v_{c1} causing capacitor voltage imbalance.

Therefore, for the GSC of WTS with the assumed sign conventions depicted in Fig. 1, the OS fault in either of the switches $S^g_{a_1}$ and $S^g_{a_2}$ blocks the negative half cycle of i^g_a (current direction from dc-link to grid); on the other hand, the fault in either $S^g_{a_3}$ or $S^g_{a_4}$ OS fault makes the positive half cycle of i^g_a to be blocked. The signal attributes of various OS fault in GSC under UPF are depicted in Fig. 6(a)–(d). Unlike the MSC

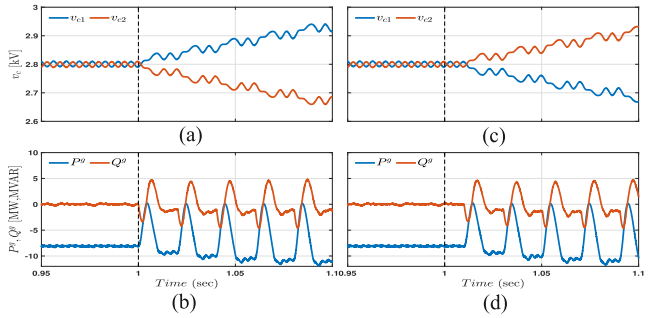

Fig. 7. GSC signal responses: (a) Capacitor voltages, (b) active and reactive power responses with outer-switch fault, (c) capacitor voltages, and (d) active and reactive power responses with inner-switch fault.

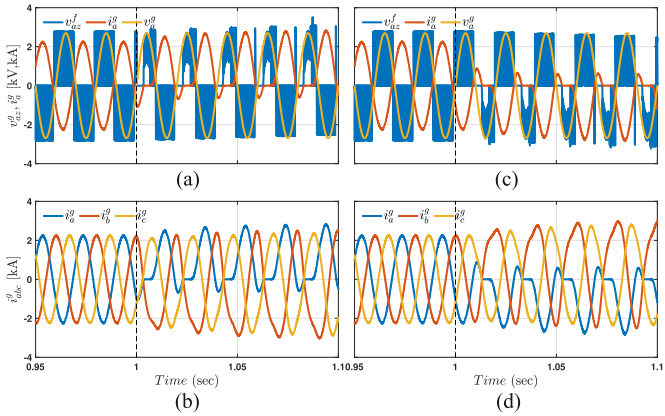

Fig. 8. GSC signal attributes under NUPF: (a) and (b) Pole voltage and currents during $S^g_{a_1}$ fault, and (c) and (d) pole voltage and currents during $S^g_{a_4}$ fault.

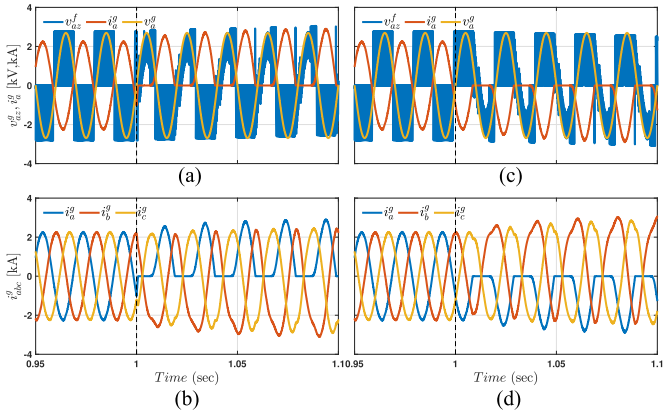

Fig. 9. GSC signal attributes under NUPF: (a) and (b) Pole voltage and currents during $S^g_{a_2}$ fault, and (c) and (d) pole voltage and currents during $S^g_{a_3}$ fault.

OS faults, the GSC OS fault entirely blocks any one of the positive/negative half cycles of respective phase current with increased distortions in remaining phase currents. In addition, the capacitor voltage imbalance during the GSC OS fault is much evident in Fig. 7(a) and (c). Further, the distorted currents cause considerable pulsations in the active and reactive power injected into the grid, as pictured in Fig. 7(b) and (d).

In most WTS applications, the GSC converters may be required to operate with NUPF based on grid code. Under such conditions, the effect of OS fault in the GSC parameter attributes is distinguishable from UPF operation. Therefore, OS fault in GSC with NUPF is analyzed. With NUPF, the switching state $[P]$ is blocked by the $S^g_{a_1}$ fault, however, the switching state $[O]$ can forward bias the diode $D^g_{ca_1}$ until the grid voltage reaches from negative to zero. Therefore, a path exists as in Fig. 2(b) for a short duration with the current $i_y < 0$. Then, as soon as the grid voltage becomes positive the current decays to zero and no path exists for current flow. Similarly, the switching state $[N]$ is blocked by the fault in $S^g_{a_4}$ and the $D^g_{ca_2}$ provides a path for current $i_y > 0$ as in Fig. 2(b) for a short duration until the grid voltage reverse biases the $D^g_{ca_2}$. As a result, based on the sign conventions of WTS shown in Fig. 1, a smaller part of the negative and positive half cycles are conducted, respectively, for the fault in the $S^g_{a_1}$ and $S^g_{a_4}$ switches. The signal attributes can be inferred from Fig. 8(a) to (d). Besides, the inner-switch faults ($S^g_{a_2}$ and $S^g_{a_3}$) make the switching state $[O]$ not possible, the entire negative and positive half cycles are blocked. The signal features are given in Fig. 9(a)–(d), further, the fault under NUPF also causes the capacitor voltage unbalancing and power fluctuations.

From the Sections II-A and II-B, the OS fault in any of the legs of the BTB converter initiates specific fluctuations in operating currents, causes speed and torque pulsations, and severe capacitor voltage unbalancing. Therefore, an effective fault diagnosis method is essential to increase the reliability and availability of WTS.

III. Proposed Fault Diagnosis Method

Each of the phase currents of the PMSG machine can have four different current patterns under OS fault in the switches $S^m_{y_1}$, $S^m_{y_2}$, $S^m_{y_3}$, and $S^m_{y_4}$ for any of the legs in MSC. Besides, the GSC's operating power factor determines the current pattern in the phase in which the OS fault occurs. As discussed in Section II, the current pattern remains identical for inner-switch faults regardless of the power factor. On the other hand, for NUPF, the current pattern for inner and outer-switch faults is different. Therefore, each converter requires unique localization methods.

A. MSC OS Fault Detection and Localization

The nonlinear nature and complex dynamics of WTS have rapid fluctuations in operating parameters during a fluctuating wind speed. Moreover, the operating speed requires fast dynamic tracking for maximum power extraction operation. Hence, the fault diagnosis method should be designed to be robust against the erroneous indications resulting from the speed and other parameter transients. The proposed fault detection and localization method utilize the main control scheme's instantaneous phase currents and capacitor voltages without additional sensors. The measured signals are availed from the vector control scheme and used in fault detection algorithms after passing through a low pass filter (LPF) with a cut-off frequency of 200 Hz [23], [31]. Nevertheless, the estimation and load current averaging

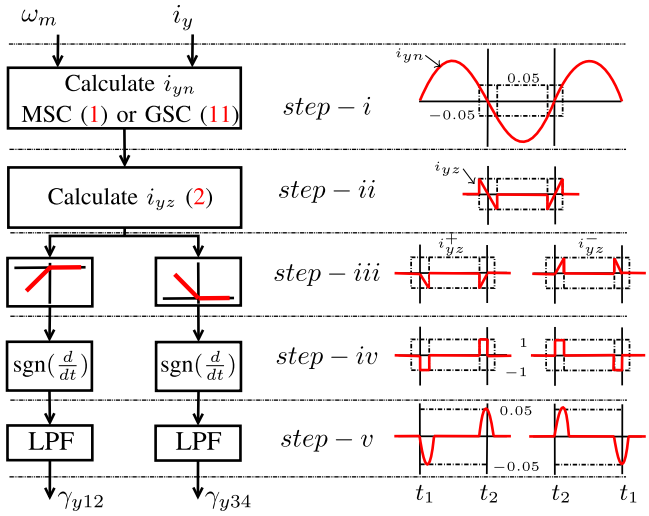

Fig. 10. Step-by-step formulations and signal features under normal operations.

methods reported in the literature are not taken to ensure minimal calculations and less computational requirement.

The OS fault in the MSC has minimal distortions in phase currents. Since the MSC operates as a rectifier and takes its current path through free-wheeling diodes, the distorted phase currents remain at zero for a short period. Moreover, the zero period for any outer-switch fault ($S^m_{y_1}$ and $S^m_{y_4}$) is much shorter than for the inner-switches ($S^m_{y_2}$ and $S^m_{y_3}$). The proposed detection method utilizes the derivative of normalized phase currents when it remains near the zero value. The step-by-step formulations for MSC OS fault detection are given in Fig. 10. In $step-i$, the normalized phase currents i_{yn} are calculated from the instantaneous phase currents as follows:

$$i_{yn} = \frac{i^m_y}{|\hat{i}^m_q|} \tag{1}$$

where $y \in (a, b, c)$ and $\hat{i}^m_q$ is the PMSG q-axis current, it can be approximated as $\hat{i}^m_q = \frac{k_{opt}\omega^2_m}{1.5p\phi}$ based on Remark 1. In which, k_{opt} is the optimum torque constant of the WTS controller, ω_m is the rotor speed, p is the generator pole pairs, and ϕ is the air gap magnetic flux [32].

Remark 1: During the OS fault, the distorted phase currents affect the phase-locked loop approximation of the dq-axes current to a greater extent. This may introduce severe errors in current normalization, and consequently, erroneous fault alarm and localization may be initiated. On the other hand, the ω_m has much lower distortions due to OS faults. Therefore, the approximation of $\hat{i}^m_q$ in current normalization uses the information of rotor speed.

In our study, 5% of the maximum amplitude of the instantaneous current is taken as ZRV. Generally, the generator of WTS operates with variable speed to ensure the maximum power extraction according to the varying wind velocity. As a result, the stator phase currents also vary with the operating speed [33]. In the proposed OS fault diagnosis method, the varying phase currents of any amplitude should be down-scaled to have an instantaneous +ve and -ve maximum as +1 and −1, respectively. With this, a generalized ZRV can be formulated between the band limit of 0.05 and −0.05. Therefore, the actual value of instantaneous phase currents should be normalized to have a +ve and -ve maximum as +1 and -1, respectively. Generally, with zero direct axis current control of PMSG-based WTS, the i^m_d is kept at zero, and the $\hat{i}^m_q$ current is equal to the maximum amplitude of instantaneous phase currents of the machine [34]. Therefore, the normalization of phase currents between +1 and −1 is done by dividing the phase currents by $|\hat{i}^m_q|$ in (1).

Then, in $step-ii$, a ZRV i_{yz} is defined based on the following conditions:

$$i_{yz} = \begin{cases} i_{yn} & \text{for} \quad \text{abs}(i_{yn}) < 0.05 \\ 0 & \text{for} \quad \text{abs}(i_{yn}) \geq 0.05. \end{cases} \tag{2}$$

Then, in $step-iii$, a clipping operation is performed as follows:

$$i^+_{yz} = \begin{cases} i_{yz} & \text{for} \quad i_{yz} < 0 \\ 0 & \text{for} \quad i_{yz} \geq 0 \end{cases}; \; i^-_{yz} = \begin{cases} i_{yz} & \text{for} \quad i_{yz} > 0 \\ 0 & \text{for} \quad i_{yz} \leq 0 \end{cases} \tag{3}$$

the i^+_{yz} is used to calculate the detection variable of $S^m_{y_1}$ and $S^m_{y_2}$. Besides, the i^-_{yz} is used for the fault detection variable of $S^m_{y_3}$ and $S^m_{y_4}$. Further, the $step-iv$ identifies the sign of the derivative of clipped currents and then the signal is passed to the LPF in $step-v$. The final output from $step-v$ is the detection variables γ_{y12} and γ_{y34} for fault alarm and switch localization. The signal features of each of the above steps under normal operation are depicted in Fig. 10. The zero crossing of currents from positive to negative occurs at the instant t_1 and the negative to positive occurs at t_2. In $step-iii$, the clipped-off response of i^+_{yz} is linearly decreasing near t_1 and linearly increasing near t_2. consequently, the $step-iv$ output has a single negative pulse near t_1 and a positive pulse near t_2. On the other hand, i^-_{yz} in $step-iii$ is linearly increasing near t_1 and linearly decreasing near t_2. Hence, the $step-iv$ output has a single positive pulse near t_1 and a negative pulse near t_2. Then, the LPF in $step-v$ calculates detection variable γ by attenuating the high-frequency noise introduced by the derivative. The cut-off frequency of LPF is set to six times higher than the rated frequency, and the LPF design procedure is discussed follows:

Generally, the phase current's fundamental frequency is denoted as f_f; and the fundamental period is calculated as $T_f = \frac{1}{f_f}$. Then, as depicted in the Fig. 11, the period for which the abs(i_{yn}) <0.05 (the period of ZRV T_{ZRV}) can be approximated as follows:

$$\frac{T_{\text{ZRV}}}{2} = \frac{\sin^{-1}(0.05) \times T_f}{2\pi}. \tag{4}$$

Then, for a sampling rate f_s, the sampling period can be calculated as $T_s = 1/f_s$. With the above parameters, the LPF in $step-iv$ is designed based on the principle of moving average finite impulse response filtering [35]. It can be formulated as

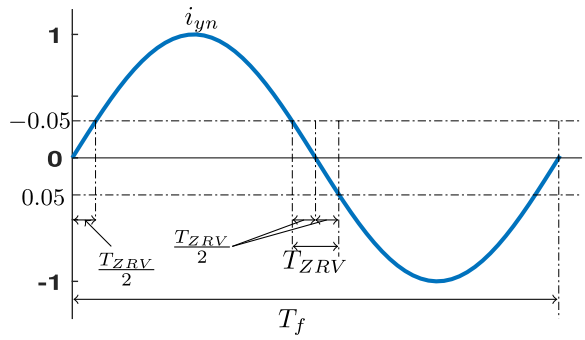

Fig. 11. Illustration of ZRV timing calculations.

follows:

$$y(k) = \frac{1}{N+1}\sum_{i=0}^{N} x(k-i) \tag{5}$$

where N is the order of the filter, the value of N is selected based on the number of samples h taken within the period T_{ZRV}. Generally, for constant frequency operation, as in the case of the grid side converter (GSC), the T_{ZRV} remains fixed. However, the fundamental frequency of i_{yn} at the machine-side converter increases (MSC) with the WTS operating speed. Therefore, the T_{ZRV} remains larger for low-frequency operation and decreases with the increased operating speed. Hence, the order of filter N should be selected by considering the lower cut-off value of the operating speed and fundamental frequency. Moreover, the T_{ZRV} is calculated by substituting the fundamental period of the least possible stator current frequency from the WTS specifications. Then, the number of samples h within the T_{ZRV} is calculated as follows:

$$h = \frac{T_{\text{ZRV}}}{T_s}. \tag{6}$$

Then, the order of the filter is taken as $N > h$. Further, the detection variable γ is derived by passing the output $y(k)$ to the moving mean function to attenuate the high-frequency noise introduced by the derivative operator

$$\gamma(k) = \sum_{i=0}^{W} y(k-i) \tag{7}$$

where W is the window length of the moving mean function. The value of W is usually selected as T_f/T_s. The above-generalized design procedure is adapted to formulate the LPFs in Algorithms 1 and 2 by utilizing the information of the fundamental time period of i_{yn} and sampling period.

The γ usually ranges from -0.05 to 0.05 for the 10 MW-PMSG WTS parameters and satisfy the condition $\gamma^{-l} < \gamma < \gamma^{l}$ under normal operation. The γ^{-l}, γ^{l} are the -ve and +ve lower thresholds to detect the OS faults.

Then, the signal features of fault detection steps during the occurrence of a fault are depicted in Fig. 12. The response of detection variable γ for fault in outer-switches S^m_{y1} and S^m_{y4} is given in Fig. 12(a) and (b), respectively. The ZRV response of S^m_{y1} fault causes few pulses at $step - iv$ with larger negative

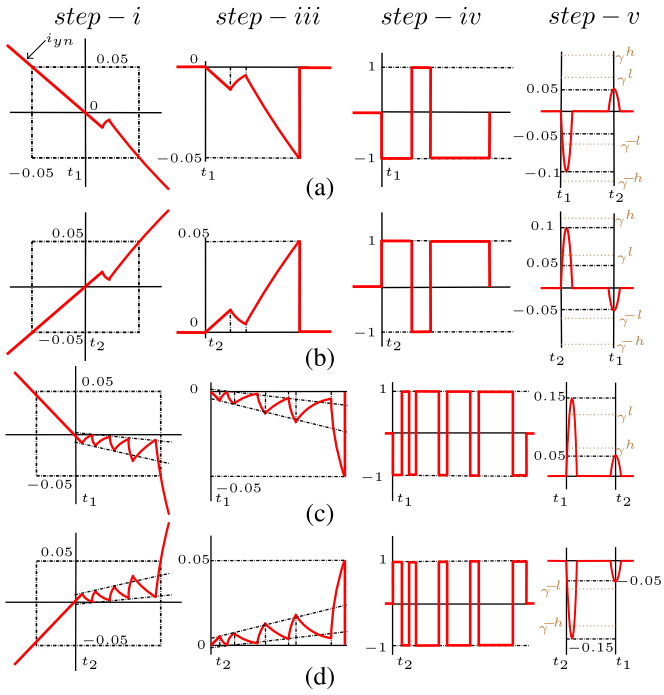

Fig. 12. Signal features of fault detection steps under OS fault in (a) S^m_{y1}, (b) S^m_{y4}, (c) S^m_{y2}, and (d) S^m_{y3}.

duration and shorter positive duration near the instant t_1. As a result, the γ_{y12} response starts to jump up to -0.1, hence going below the -ve lower threshold γ^{-l}. Besides, the ZRV response of S^m_{y4} fault causes few pulses at the $step - iv$ with larger positive duration and shorter negative duration near the instant t_2. As a result, the γ_{y34} response starts to jump up to 0.1 and go above the +ve lower threshold γ^{l}.

Further, the signal features for fault in inner-switches S^m_{y2} and S^m_{y3} are depicted in Fig. 12(c) and (d). The ZRV response has sustained ripples near the zero current for a specific duration. Consequently, the output produced at $step - iv$ has more pulses compared to outer-switch faults. Moreover, the current ripples cause larger positive pulses for S^m_{y2} fault and larger negative pulses for S^m_{y3} fault. In both cases, the pulse frequency is higher than the outer-switch faults; as a result, the γ_{y12} goes up to 0.15 for S^m_{y2} fault and hence reaches the +ve upper threshold γ^{h}. Besides, γ_{y34} reach up to -0.15 under S^m_{y3} fault and comes below the -ve upper threshold γ^{-h}. Thus, under normal operating conditions, the detection variable γ_{y12}, and γ_{y34} vary between ± 0.05 which is lower than the limits of lower thresholds, whereas, under various OS faults, the γ values of the corresponding phase crosses the threshold values as $[\gamma^{-h} = -0.12, \gamma^{h} = 0.12, \gamma^{-l} = -0.06, \gamma^{l} = 0.06]$.

In addition, it can be noted that the OS fault in the inner switches initiates the capacitor voltage unbalancing to a considerable value. Based on the faulty inner-switch, the fault confirmation variable δ_c can be formulated as follows:

$$\delta_c = \frac{v_{c1} - v_{c2}}{v^*_{dc}} \tag{8}$$

Algorithm 1: MSC Fault Detection and Localization.

Step 1: Get the values of γ_{y12}, γ_{y34}, and δ_c
Step 2: Fault Identification.
if abs(γ_{y12})||abs(γ_{y34}) $< \gamma^{l}$ **then**
Go to Step 1;
else
Trigger Fault Alarm and Go to Step 3;
end if
Step 3: Begin Fault Localization.
if $\gamma_{y12} > \gamma^{h}$&&$\delta_c < -0.05$ **then**
Faulty switch=$S^{m}_{y_2}$;
else if $\gamma_{y12} < \gamma^{-l}$ **then**
Faulty switch=$S^{m}_{y_1}$;
else if $\gamma_{y34} < \gamma^{-h}$&&$\delta_c > 0.05$ **then**
Faulty switch=$S^{m}_{y_3}$;
else if $\gamma_{y34} > \gamma^{l}$ **then**
Faulty switch=$S^{m}_{y_4}$;
else
Go to Step 3 (recheck);
end if

δ_c has the attribute of $\delta_c < -0.05$ for $S^{m}_{y_2}$ fault and $\delta_c > 0.05$ for $S^{m}_{y_3}$ fault. Finally, the Algorithm 1 exemplifies the detection of OS fault and localization of faulty switches by utilizing the detection and confirmation variables.

Remark 2: The OS fault in $S^{m}_{y_3}$ causes the current to remain zero for a particular duration at the instant t_2. The fluctuating current near the zero value will have a few spikes reaching the negative side, reflected in the ZRV of γ_{y12} calculations. As a consequence, the pulses are produced at the output of $step - iv$ with larger positive duration, and hence the γ_{y12} jump up to 0.08 which is higher than the γ^{l}. On the other hand, the fault in $S^{m}_{y_2}$ causes the opposite effect and makes the γ_{y34} to reach up to $-0.08 < \gamma^{-l}$. This phenomenon should be carefully considered in designing the localization algorithm by avoiding the usage of γ_{y12} range γ^{l} to γ^{h}, and γ_{y34} range γ^{-h} to γ^{-l} for threshold setting.

B. GSC OS Fault Detection and Localization

The GSC operates as a VSI and injects the active and reactive power into the grid through inductive filters. Voltage-oriented control is employed by aligning the d-axis voltage of GSC to the magnitude of grid voltage v^{g}_{y} and q-axis voltage is kept at zero [32]. As a result, the switching states $[P]$ and $[N]$ are vital to synchronize the phase current into grid voltage. For example, the OS fault in $S^{g}_{y_1}$ or $S^{g}_{y_2}$ switch affects these switching states and blocks the entire negative half cycle (based on assumed sign convention) under UPF operation. On the other hand, the NUPF operation allows a little current into the negative side for $S^{g}_{y_1}$ fault and blocks the entire cycle for $S^{g}_{y_2}$ fault. Hence, the OS fault in the GSC initiates higher distortions in phase currents than in the MSC. Moreover, the signal attributes of currents under UPF operation are identical for both inner and outer-switch faults. Hence makes it difficult to localize the faulty switch with conventional methods. However, the proposed method with ZRV can distinguish the different types of faults by observing the ripples of currents near the zero value, as explained in the previous section. Hence, the step-by-step formulations in Fig. 10 can also be adapted to GSC fault identification and localization with the modified i_{yn} and threshold values.

TABLE I
RANGE OF γ FOR OS FAULTS IN GSC

Switch	γ_{y12}	γ_{y34}	δ_c
$S^{g}_{y_1}$	0 to 0.22	-0.15 to 0	> 0.05
$S^{g}_{y_2}$	0 to 0.25	-0.1 to 0.15	> 0.05
$S^{g}_{y_3}$	-0.15 to 0.1	-0.25 to 0	< -0.05
$S^{g}_{y_4}$	0 to 0.15	-0.22 to 0	< -0.05

Remark 3: The GSC phase currents are the vector sum of dq-axes currents. Generally, the q axis current injects the active power, and the d-axis current injects the reactive power; hence, the grid current normalization should consider both the dq-axes currents. Moreover, during the OS fault, the distorted phase currents affect the phase-locked loop approximation of the dq-axes current to a greater extent. This may result in an erroneous fault alarm and localization. Besides, the OS fault in GSC does not affect the operating speed of the generator. Therefore, this study introduces an equivalent MSC to GSC q-axis current (active power components of both the converters) transformation to normalize grid currents as follows:

$$|1.5 v^{g}_{q} i^{g}_{q}| \approx |1.5 v^{m}_{q} \hat{i}^{m}_{q}| \tag{9}$$

$$\hat{i}^{g}_{q} \approx \left(\frac{v^{m}_{q}}{v^{g}_{q}}\right) \frac{k_{\text{opt}} \omega^{2}_{m}}{1.5 p \phi} \tag{10}$$

where $\hat{i}^{g}_{q}$ is the GSC equivalent of $\hat{i}^{m}_{q}$ calculated by using rotor speed information, and v^{g}_{q}, v^{m}_{q} are q-axis grid and machine voltages.

Therefore, based on Remark 3, the normalized currents for GSC fault identification can be calculated in $step - i$ as follows:

$$i_{yn} = \frac{i^{g}_{y}}{\sqrt{(\hat{i}^{g}_{q})^2 + (i^{g*}_{d})^2}}. \tag{11}$$

Then, the remaining steps are followed as explained for MSC fault detection, and finally, the $\gamma_{y12}, \gamma_{y34}$ are availed at $step - v$. After that, the threshold values are identified based on the switching frequency and filter parameters. Besides, the δ_c is approximated with (8) and Algorithm 2 is formulated by identifying the threshold values $[\gamma^{-h} = -0.2, \gamma^{h} = 0.2, \gamma^{-l} = -0.1, \gamma^{l} = 0.1]$ by using the range of γ given in Table I specifically for the different switch faults of 10 MW system.

Based on the Algorithms 1 and 2, Fig. 13 illustrates the block schematic of the proposed OS fault diagnosis and localization scheme. The operating parameters $[i^{m}_{abc}, i^{g}_{abc}, \omega_m, v_{c1}, v_{c2}, v^{m}_{q}, v^{g}_{q}]$ are availed from MSC/GSC vector control to realize the proposed scheme.

Algorithm 2: GSC Fault Detection and Localization.

Step 1: Get the values of γ_{y12}, γ_{y34}, and δ_c
Step 2: Fault Identification.
if abs(γ_{y12})||abs(γ_{y34}) $< \gamma^{l}$ **then**
Go to Step 1;
else
Trigger Fault Alarm and Go to Step 3;
end if
Step 3: Begin Fault Localization.
if $\gamma_{y12} > \gamma^{h}$&&$\delta_c > 0.05$ **then**
Faulty switch=$S^m_{y_1}$;
else if $\gamma_{y12} < \gamma^{-l}$&&$\delta_c < -0.05$ **then**
Faulty switch=$S^m_{y_3}$;
else if $\gamma_{y34} < \gamma^{-h}$&&$\delta_c < -0.05$ **then**
Faulty switch=$S^m_{y_4}$;
else if $\gamma_{y34} > \gamma^{l}$&&$\delta_c > 0.05$ **then**
Faulty switch=$S^m_{y_2}$;
else
Go to Step 3 (recheck);
end if

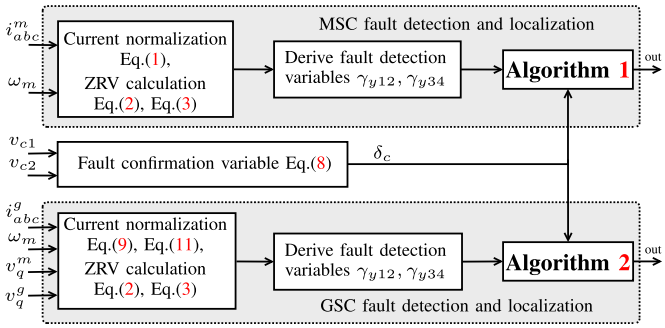

Fig. 13. General block schematic of proposed fault diagnosis scheme.

IV. Simulation and Hardware Implementation

A. Simulation Results

1) 10MW PMSG-Based WTS: The proposed method is verified by simulation of 10MW PMSG-based direct-drive WTS equipped with NPC BTB full-scale power converter. The detailed configuration, control principle for MSC, and control of GSC are referred from [7], and the machine, aerodynamic, and grid parameters are given in Table III. The modeling and simulation of the WTS and proposed fault diagnosis method were done in MATLAB/Simulink environment. The OS fault in the required switches is instigated by blocking the gate pulses.

The simulation results of the MSC parameters such as rotor speed ω_m, phase currents i^m_{abc}, and fault detection and localization variables $\gamma_{y12}, \gamma_{y34}$ during a transient WTS aerodynamic torque T_{ad} and OS fault occurrences in MSC are presented in Fig. 14. To substantiate the reliability and immunity to erroneous fault alarms, a transient aerodynamic torque is considered similar to [21]. The T_{ad} is increasing from 10% to the rated value at 0.5 s. Then, the T_{ad} is suddenly reduced to 10% at 0.75 s, and finally, at 1.1 s, it increases to 90% of rated value.

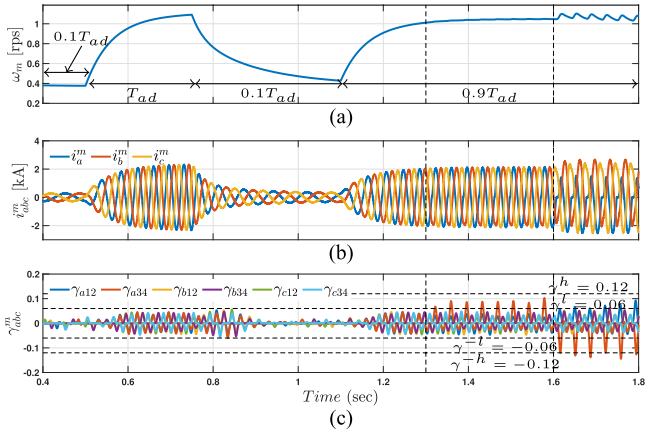

Fig. 14. Simulation results under OS faults in $S^m_{a_3}$ and $S^m_{a_4}$, (a) rotor speed, (b) phase currents, and (c) detection variable γ.

The response of rotor speed and phase currents are shown in Fig. 14(a) and (b). During such transients, it can be noted that the detection variables in Fig. 14(c) are well below the threshold even for the step change in torque of 90%. In contrast, in real WTS, no such high-magnitude transient is practically possible. Therefore, the immunity to erroneous fault alarms due to load variations is verified. Furthermore, it is essential to note that, as a consequence of the reduction of load at 0.75 s, the detection variables γ_{y12} are going beyond 0.05 and γ_{y34} are coming below -0.05. If the criterion given in Remark 2 is not considered in the detection and localization, this may lead to the misinterpretation of transients as a fault. Therefore, selecting the threshold for fault detection and localization is crucial.

Further, to evaluate the diagnostic performance of the proposed system, OS faults are initiated, during which the torque is maintained at 90% of T_{ad}. Initially, an outer-switch fault is triggered at the instant 1.3 s in $S^m_{a_4}$, and the inner-switch open fault is initiated at 1.6 s in $S^m_{a_3}$. The occurrence of $S^m_{a_4}$ OS fault distorts the i^m_a near the zero crossing from negative to positive, as depicted in Fig. 3(c). Meanwhile, the diagnostic variable γ_{a34} jumps above the threshold γ^{l}, allowing the Algorithm 1 to detect and localize the faulty switch as $S^m_{a_4}$. Then, at 1.6 s, further prolonged distortions near zero crossing are noted due to inner-switch fault, as pictured in Fig. 4(c). Consequently, the variable γ_{a34} comes below γ^{-h}, so the fault in $S^m_{a_3}$ is detected. At this time, it can be noted that the zero crossing of ZRV i_{az} makes the γ_{a12} to jump above γ^{l} (see Remark 2), as shown in Fig. 14(c). Since the range is cautiously avoided for localization of fault in $S^m_{y_1}$, and $S^m_{y_2}$, misinterpretation is avoided. Moreover, in both cases, the time taken to detect the fault from the first zero crossing after the fault occurrence is less than 30% of the fundamental period of phase current.

Then, regarding the GSC, similar faults are considered at the same instants in switches $S^g_{b_4}$ and $S^g_{b_3}$ with healthy MSC switches. The results are analyzed for UPF and NUPF operation, and the same aerodynamic load conditions are maintained. The response of current and γ is given for UPF and NUPF, respectively, in Figs. 15(a) and (b) and 16(a) and (b). In both cases, the

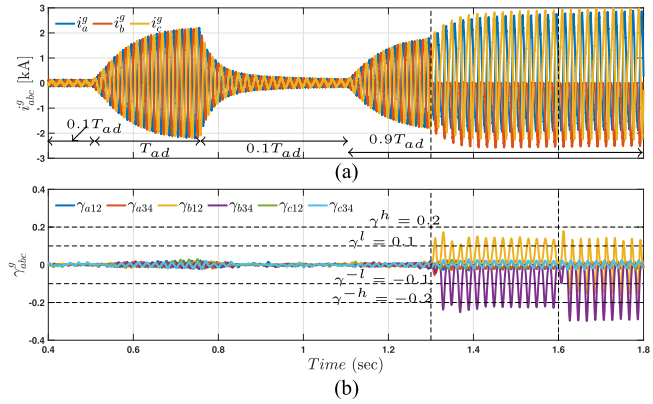

Fig. 15. Simulation results under OS faults in $S_{b_3}^g$ and $S_{b_4}^g$ under UPF (a) phase currents, and (b) detection and localization variable γ.

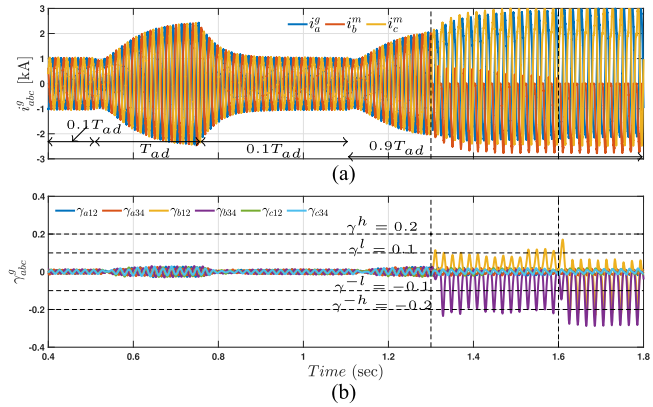

Fig. 16. Simulation results under OS faults in $S_{b_3}^g$ and $S_{b_4}^g$ under NUPF (a) phase currents, and (b) detection and localization variable γ.

TABLE II
THRESHOLDS FOR OS FAULT DETECTION IN 10MW AND 5 KW WTS

Threshold	10MW WTS		5kW WTS	
	3L MSC	3L GSC	3L MSC	3L GSC
γ^h	0.12	0.2	0.13	0.3
γ^l	0.06	0.1	0.08	0.15
γ^{-l}	-0.06	-0.1	-0.08	-0.15
γ^{-h}	-0.12	-0.2	-0.13	-0.3

γ_{b34} reaches γ^{-h} under $S_{b_4}^g$ fault and γ_{b12} reaches γ^{-l} for $S_{b_3}^g$ fault, enabling Algorithm 2 to localize the faulty switches based on the thresholds given in Table II.

2) 5 kW *PMVG-Based WTS:* Next the proposed method is verified in a 5 kW PMVG-based WTS with NPC BTB converter. The machine, aerodynamic, and grid parameters are given in Table III. Similar to the 10 MW rated WTS, the reliability and immunity to the fault alarm are verified under transient aerodynamic torque T_{ad}.

The MSC parameters, rotor speed ω_m, capacitor voltages v_{c1}, v_{c2}, phase currents i_{abc}^m, and fault detection and localization variables $\gamma_{y12}, \gamma_{y34}$ during a transient WTS aerodynamic torque T_{ad} and OS fault occurrences in MSC are presented in Fig. 17. Based on the cut-in wind speed of 5 kW WTS, the minimum T_{ad}

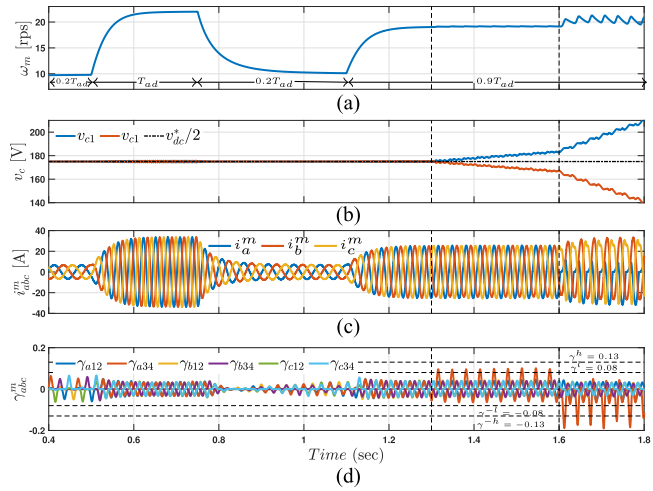

Fig. 17. Simulation results under OS faults in $S_{a_3}^m$ and $S_{a_4}^m$, (a) rotor speed, (b) capacitor voltages, (c) phase currents, and (d) detection variable γ.

is taken as 20% until 0.5 s and increased to rated value. Then, the T_{ad} is suddenly reduced to 20% at 0.75 s, and finally, at 1.1 s, it increases to 90% of rated value. The responses of rotor speed, capacitor voltages, and phase currents are pictured in Fig. 17(a)–(c), respectively. The responses of detection variables during the T_{ad} transients are pictured in Fig. 17(d). Unlike the MW class wind turbine, the 5 kW WTS has lower inertia. Therefore, the rotor speed accelerate/decelerate quickly and reaches to the new steady state within a short duration. This phenomenon affects the detection variable γ. In addition, the vector control of low power WTS operates with higher switching frequency and increased sampling rate. Therefore, the LPF design and threshold setting are evaluated by accounting this factors. Table II gives the threshold values for fault detection and localization, which is slightly different from the MW WTS. From the response plot Fig. 17(d), the detection variables are within the thresholds during the T_{ad} transients. Therefore, the immunity to erroneous fault alarms due to load variations is verified.

Next, the applicability of proposed scheme to the 5 kW WTS is evaluated by initiating the OS fault in switches $S_{a_4}^m$, $S_{a_3}^m$, respectively, at the instants 1.3 s and 1.6 s. During which the WTS is operated with 90% of rated T_{ad}. As discussed in MW WTS simulation results, the fault in $S_{a_4}^m$ affects the i_a^m pattern near the zero crossing from negative to positive. Consequently, the diagnostic variable γ_{a34} reaches to the threshold γ^l as pictured in Fig. 17(d). In addition, a small drift in the capacitor voltages is initiated as pictured in Fig. 17(b). As a result, Algorithm 1 detects and localize the faulty switch $S_{a_4}^m$. Further, the inner switch fault in $S_{a_3}^m$ instigates a prolonged distortions near zero crossing. Therefore, the γ_{a34} comes below γ^{-h} as shown in Fig. 17(d). In addition, the inner switch fault introduces a higher capacitor voltage imbalance and causes the $|\delta_c| > 0.05$. Consequently, the fault in $S_{a_3}^m$ is detected by the Algorithm 1. Similar to the MW WTS results, the time taken to detect the fault after the occurrence is less than 30% of the fundamental period.

Further, identical faults are considered at the instants 1.3 s, 1.6 s in switches $S_{b_4}^g$ and $S_{b_3}^g$ with healthy MSC switches. The

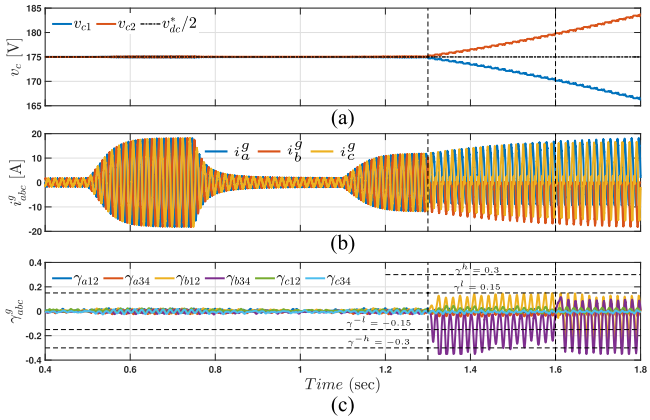

Fig. 18. Simulation results under OS faults in $S^g_{b_3}$ and $S^g_{b_4}$ under UPF (a) capacitor voltages, (b) phase currents, and (c) detection and localization variable γ.

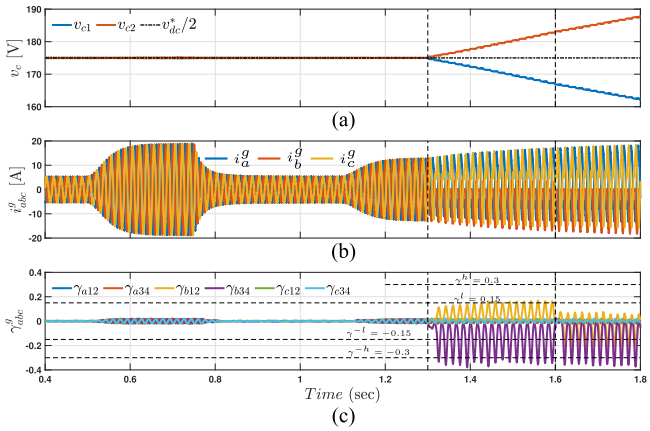

Fig. 19. Simulation results under OS faults in $S^g_{b_3}$ and $S^g_{b_4}$ under NUPF (a) capacitor voltages, (b) phase currents, and (c) detection and localization variable γ.

results are pictured for UPF and NUPF operation, and the same aerodynamic load conditions are maintained. The responses of capacitor voltages, current, and γ are given for UPF, respectively, in Fig. 18(a), (b), (c). Then, Fig. 19(a), (b), and (c) pictures the responses of NUPF operation. In each case, the Algorithm 2 localizes the faulty switches based on the δ_c and thresholds given in Table II. Therefore, from the 10 MW and 5 kW WTS results, the applicability, reliability, and robustness of the proposed scheme for OS fault detection and localization are verified for low power and high power WTSs.

B. Experimental Verification

In this section, the proposed method has been validated by implementing it in a grid-connected 3 L BTB NPC converter experimental setup to interface a 5-kW rated PMVG driven by a wind turbine emulator. The operating parameter of WTS is referred from [30]. Fig. 20 shows the 3 L BTB NPC converter-based PMVG WTS experimental setup used to test the proposed method and the specifications are tabulated in Table III.

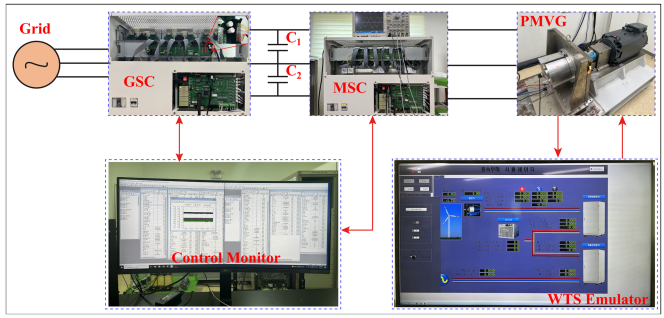

Fig. 20. Experimental setup of 5 kW 3 L BTB NPC converter fed PMVG-based WTS.

TABLE III
PARAMETERS OF SIMULATION AND EXPERIMENTAL SYSTEM SETUP

Parameter	Description	Value	
		10MW WTS [37] (Simulation)	5kW WTS [36] (Experiment)
	Grid		
V_g (V)	RMS Grid voltage	3300	220
I_g (A)	RMS Grid current	1750	12.5
L_f (mH)	Filter inductance	1.2	10
	Wind turbine		
R_b (m)	Rotor Blade Radius	85	2.8
λ_{opt}	Optimal tip speed ratio	8.1	6.912
$V_{w,i}$ (m/s)	Cut-in wind speed	2.5	3
$V_{w,r}$ (m/s)	Rated wind speed	11.7	9
$V_{w,m}$ (m/s)	Cut-off wind speed	25	18
$C_{p_{max}}$	Power coefficient	0.453	0.4412
k_{opt}	OTC constant	7.28e^6	0.459
	Generator		
J (Nm)	Rotor inertia	40e^6	1.18
n_r (rpm)	Rated rotor speed	10	213
p	Stator pole pairs	165	10
ϕ (Wb)	Stator magnetic flux	15.34	0.4459
L_m (mH)	Stator inductance	2.76	17.5
R_m (mΩ)	Stator resistance	97.7	400
f_e (Hz)	Rated frequency	27.5	35.5
I_r (A)	Rated RMS current	1782	25.2
E_p (V)	Induced voltage	1874	230
	Controller		
f_s (kHz)	Switching frequency	2	10
v^*_{dc} (V)	Rated dc-link voltage	5600	350

The 3 L BTB converter is configured with 12 STARPOWER GD225HFY120C6S IGBT switching modules containing two series connected IGBT devices. In addition, 12 clamping diodes are used with two 415 μF, 1100 V/60 A rated electrolytic capacitors as a dc-link. The control strategy is executed on a dedicated Texas Instruments TMS320F28335 digital signal processor for GSC and MSC converters with a sampling frequency of 10 kHz. The DSP processor produces the complementary PWM pulses with the dead-time of 3μs and is applied to the IGBT switching devices through the Realtech three-level gate interface board. Further, eight LEM LV 25-P voltage transducers are used to measure the grid, machine, and dc-link capacitor voltages. Besides, seven LEM HAS 50-S current transducers are used, respectively, to measure the grid, machine, and dc-link currents. The Autonics E40S6-1024-6-L-5 rotary-type incremental encoder measures the rotor position used in rotor speed calculation and formulation of vector control for 3 L MSC. The phase-locked loop, dc-link

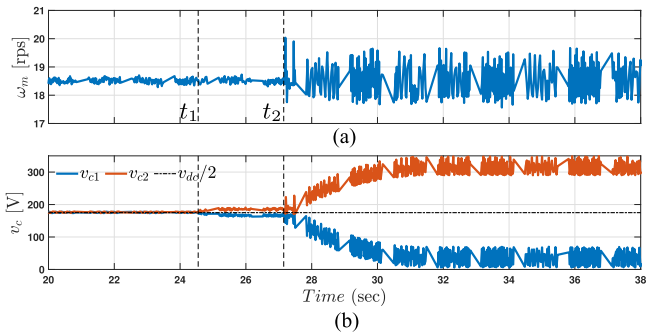

Fig. 21. Experimental results under OS faults in S^m_{a4} and S^m_{a3}, (a) rotor speed, and (b) capacitor voltages.

voltage control, current control, and grid side reactive power control are formulated based on the vector control approach described in [7].

Then, the proposed OS fault diagnosis method described in Algorithms 1 and 2 for MSC and GSC converters are implemented through DSP programming, which essentially involves the measurement of BTB converter ac side phase currents. Moreover, the threshold values of detection variables are evaluated based on the WTS and LPF parameters as tabulated in Table II. The BTB output electricity is interfaced to a 220 V, 60 Hz utility electrical grid. The aerodynamic behavior of the wind turbine is emulated through a 15-kW direct torque-controlled Siemens induction motor driven by a LabVIEW interfaced programmable logic controller. The operating parameters and control variables used in the experimental setup are referred from [36], and the OS fault is created by open circuiting the gate pulses to the IGBT devices S^m_{a4},S^m_{a3} by using mechanical push buttons shown in the zoomed part of GSC in Fig. 20.

The experimental results are availed by creating a S^m_{a4},S^m_{a3} OS fault when the WTS is operating with 90% rated aerodynamic torque T_{ad} and the response of ω_m and capacitor voltages are pictured in Fig. 21. Initially, the outer-switch OS fault is triggered at the instant of t_1 (S^m_{a4} fault), followed by the inner-switch OS fault at t_2. The response of ω_m in Fig. 21(a) indicates that there is little oscillation in rotor speed for S^m_{a4} fault and slightly noticeable rotor speed oscillations during S^m_{a3} fault, therefore justifying the usage of rotor speed information for current normalization in Remark 1 and Remark 3. Then, the response of v_c in Fig. 21(b) shows the deviation of capacitor voltages under OS faults, justifying the formulation of fault confirmation variable δ_c used in localization algorithms.

Next, the scope responses of generator phase currents under normal and faulty switch operations are depicted in Fig. 22. The i^m_{abc} responses under normal operation is shown in Fig. 22(a). Further, the initiation of outer-switch OS fault in S^m_{a4} distorts the i^m_{abc} responses as pictured in Fig. 22(b). Then, the inner-switch OS fault further distorts the phase currents as depicted in Fig. 22(c). Further, to illustrate the operation on Algorithm 1 for diagnosing the faulty switch, the current of faulty phase (phase-a) is pictured along with its fault detection variables $\gamma^m_{a12}, \gamma^m_{a34}$ and thresholds in Fig. 23. Under normal operation, the fault detection variables oscillate within the bounds of thresholds as shown in Fig. 23(a). Then, with the gate pulse to the outer-switch S^m_{a4} disabled, the γ^m_{a34} reaches to the threshold γ^l as depicted in Fig. 23(b), hence detected and localized by the Algorithm 1. Besides, the fault in S^m_{a3} alters the behavior of detection γ^m_{a34} to jump up to γ^{-h} as pictured in Fig. 23(c). At the same time, the deviation in capacitor voltage also enlarges. Therefore, detected and diagnosed by the Algorithm 1 by utilizing γ^m_{a34} and δ_c.

Then, regarding the GSC operation, the S^g_{a4} and S^g_{a3} faults are triggered with steady input power passing through the dc-link with healthy MSC switches. The results are availed under UPF operation. The phase current responses and γ are pictured, respectively, in Fig. 24(a) and (b). The instantaneous values of γ_{a34} and δ_c enable the Algorithm 2 to localize the faulty switches based on the thresholds given in Table II.

Further, experiments have been conducted to verify the reliability and immunity to erroneous fault indications under the sudden dynamic variations in WTS operating parameters. Moreover, the sudden variation in operating parameters, such as the reactive power injection to the grid Q^{g*}, dc-link voltage variation v^*_{dc}, sudden change in WTS aerodynamic torque T_{ad} may lead to highly oscillating response in phase currents of generator and grid. Since the proposed method mainly depends on the instantaneous value of currents, the variation range of the detection variable should be verified for oscillating within the threshold bounds $\gamma^{-l} < \gamma < \gamma^l$ under dynamic changes in operating parameters. The responses of phase current i^g_a, γ_{a12} and γ_{a34} under dynamic changes of different operating parameters are depicted in Fig. 25. In Fig. 25, the dotted lines indicate the bounds of threshold values γ^{-l}, γ^l.

Usually, the WTS extracts a much lower power near the cut-in wind speed. At this time, the amplitude of phase currents at the grid side has a minimum amplitude and higher level of harmonics due to the constant grid voltage [38]. Therefore it is essential to ensure that the detection variables should not erroneously identify the oscillating lower amplitude current near zero crossing as the fault current. An effective current normalization can avoid such erroneous fault indications. To verify this, the response of i^g_a and its detection variables are analyzed in Fig. 25(a) under light load operation of WTS by applying 10% of the rated load. Next, with the same light load conditions, the reactive power injection to the grid is enabled by making the $i^{g*}_d = -10$A (60% of rated grid current), and the responses are plotted in Fig. 25(b). Then, a step variation in reactive power injection is carried by making a step change in i^{g*}_d and the responses are pictured in Fig. 25(c). Next, the effect of aerodynamic torque variation over the grid current response and its detection variables is depicted in Fig. 25(d) for a step increment in T_{ad} from 50% to 80% of rated torque. Then, the T_{ad} is reduced suddenly from 80% to 50%, and the grid responses are plotted in Fig. 25(e). Next, the effect of dc-link voltage variations over the detection variables is analyzed. To do this, the dc-link voltage is varied in steps of 5 V for each 2s from 325 to 375 V ($\pm$25 V from v^*_{dc}) and the detection variable responses are plotted in Fig. 25(f). From the above response plots, it is observed that the presented current

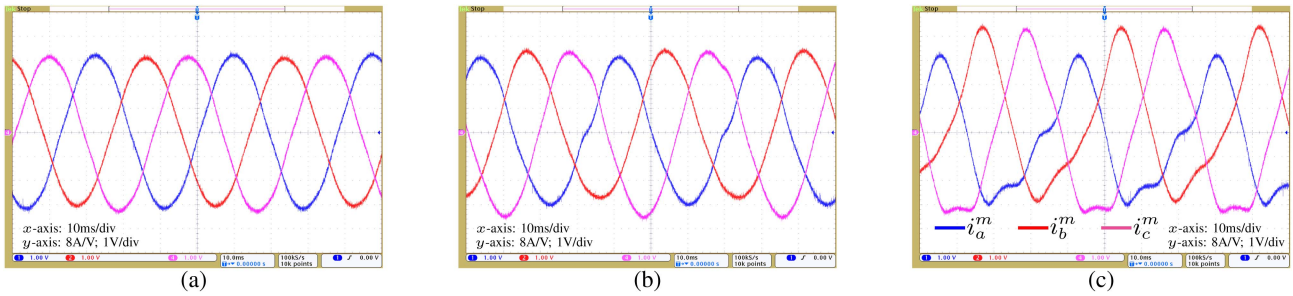

Fig. 22. MSC experimental responses of instantaneous currents i^m_{abc}: (a) Under normal operation, (b) under OS fault in S^m_{a4}, and (c) under OS fault in S^m_{a3}.

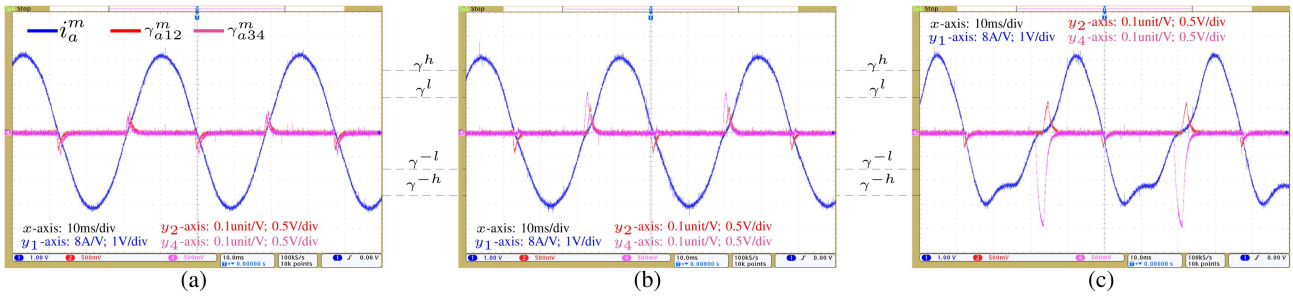

Fig. 23. MSC experimental response of phase current i^m_a and detection variables: (a) Under normal operation, (b) under S^m_{a4} fault, and (c) under S^m_{a3} fault.

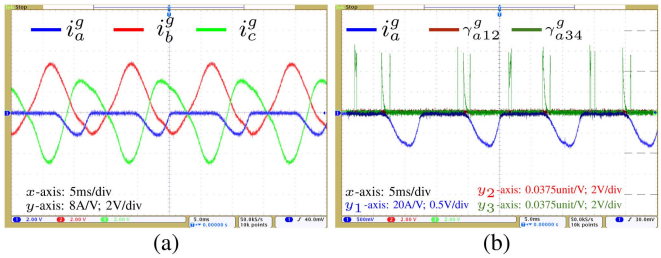

Fig. 24. GSC experimental response for OS faults. (a) i^g_{abc}. (b) i^g_a, γ_a.

normalization performs well and maintains the γ values within the thresholds and avoids erroneous fault indications under the above-said perturbations in operating parameters.

C. Robustness to Parameter Variations and Performance Comparison

The proposed method's robustness against sudden load variations has been analyzed in 10 MW PMSG-based WTS simulation, and the results are depicted in Figs. 14, 15, and 16. Further, this section aims to study the effect of ac and dc side disturbance of converters, parameter variations of PMSG machine, and grid side filter [34]. To do this, under constant load operation of the system, the GSC reactive power reference Q^{g*} is applied suddenly at 0.5 s and released at 0.75 s. Then, the machine and grid side filter inductance L_m, L_f are increased by 25% at 1 s and 1.25 s, respectively. Followed by this, the dc-link reference is increased to 5800 V at 1.5 s, and a braking resistance R_b

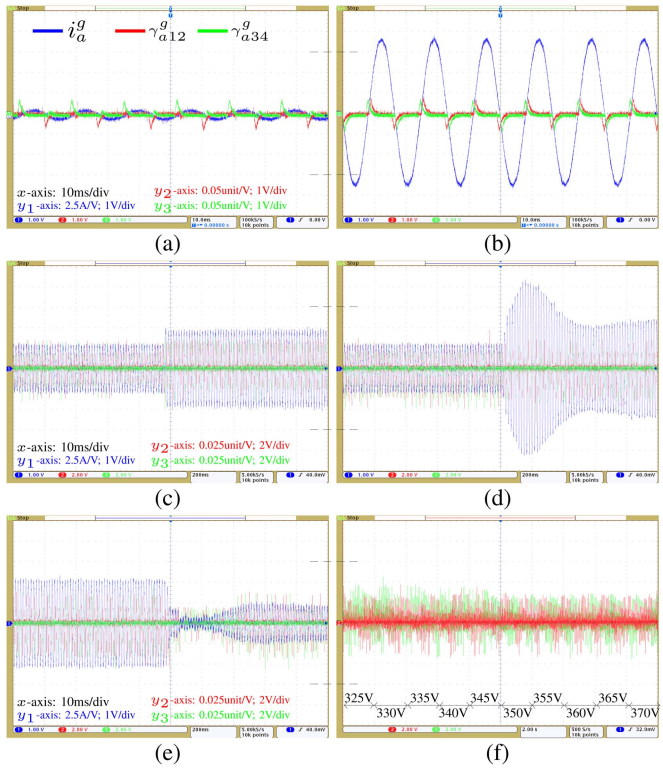

Fig. 25. GSC experimental responses i^g_{abc} and γ under, (a) light load WTS operation, (b) rated Q^{g*} injection, (c) step change in Q^{g*}, (d) step increment in WTS T_{ad}, (e) step decrement in WTS T_{ad}, and (f) variation in v^*_{dc}.

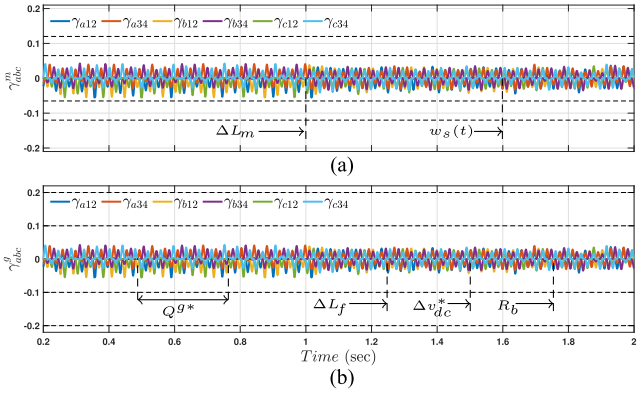

Fig. 26. Detection variables under parameter variations. (a) MSC γ^m_{abc}. (b) GSC γ^g_{abc}.

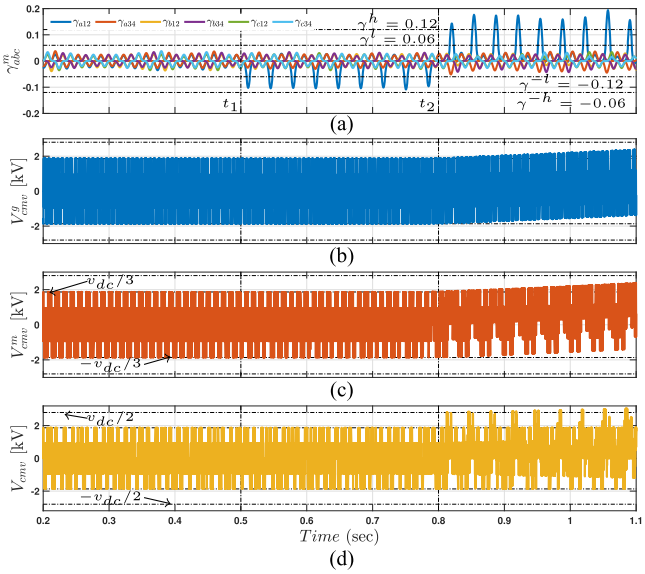

Fig. 27. Analysis of CMVs under OS fault in MSC $S^m_{a_1}$ and $S^m_{a_2}$: (a) detection variables γ^m_{abc}, (b) GSC CMV V^g_{cmv}, (c) MSC CMV V^m_{cmv} and (d) BTB converter CMV V_{cmv}.

is connected across capacitor C_2 to divert 30% of rated dc-link current at 1.75 s. In addition, a band-limited white noise $w_s(t)$ is added to the generator currents i^m_{abc} at instant 1.75 s to reflect the sensor noises. Then, the response of MSC and GSC detection variables are depicted in Fig. 26(a) and (b) respectively. The disturbances and parameter variations of the system may affect the current amplitude. However, the ripple of current near the zero range will not be affected to the extent sufficient to increase the detection variable γ.

Next, a test case is conducted to analyze the BTB NPC converter common mode voltage (CMV) under OS faults. In the schematic of WTS Fig. 1, the wye-connected phases of the grid are connected to a common point G_n, and the wye-connected PMSG phases are connected to the common point M_n. The BTB converter CMV is the voltage between the points G_n and M_n. It can also be expressed as the difference between the GSC CMV V^g_{cmv} and the MSC CMV V^m_{cmv}[39].

$$V_{\text{cmv}} = V^g_{\text{cmv}} - V^m_{\text{cmv}} = \frac{1}{3}\left(V^m_{za} + V^m_{zb} + V^m_{zc}\right) - \frac{1}{3}\left(V^g_{za} + V^g_{zb} + V^g_{zc}\right) \quad (12)$$

where $V^m_{za}, V^m_{zb}, V^m_{zc}$ are the pole voltages measured between MSC phases and the point z, and $V^g_{za}, V^g_{zb}, V^g_{zc}$ are the pole voltages measured between the GSC phases and point z. Based on (12), the CMV of a three-level NPC BTB converter may have a voltage amplitude of $[\frac{-2v_c}{3}, \frac{-v_c}{3}, 0, \frac{v_c}{3}, \frac{2v_c}{3}]$, where v_c is the capacitor voltage [40].

Based on the signal attributes of MSC and GSC for various OS faults discussed in Section II, the pole voltages are affected by the outer and inner switch OS faults. Therefore, this test case analyses the effect of OS faults over the CMV of GSC, MSC converters individually and the net CMV of the entire BTB topology. To do this, the outer and inner switch faults in the phase-a leg of the MSC ($s^m_{a_1}, S^m_{a_2}$) are triggered, respectively, at the instants t_1 and t_2 and the responses of detection variables γ^m_{abc} and CMVs $V^g_{\text{cmv}}, V^m_{\text{cmv}}, V_{\text{cmv}}$ are pictured in Fig. 27. At which, the WTS is operated with 90% of rated T_{ad}.

From Fig. 27(a), it can be observed that the OS fault at the instant t_1 makes the detection variable γ_{a12} to reach below the threshold γ^{-l}. Therefore, the Algorithm 1 detects the $s^m_{a_1}$ OS fault, similarly after the instant t_2, the γ_{a12} reaches the threshold γ^h and the $s^m_{a_2}$ OS fault is detected. The responses of CMV measured between the GSC ac side terminal and point z are pictured in Fig. 27(b). The OS fault in MSC $s^m_{a_2}$ initiates the capacitor voltage deviation by increasing $v_{c2} > v_{c1}$, therefore the V^g_{cmv} start to increase above the $\frac{2v_c}{3}$ but maintained below $\frac{v_{dc}}{2}$. On the other hand, the CMV of MSC is distorted by the $S^m_{a_2}$ OS fault as pictured in Fig. 27(c), however, still maintained below the $\frac{v_{dc}}{2}$. In contrast, the BTB CMV V_{cmv} reaches to the $\frac{v_{dc}}{2}$ instantly after the $S^m_{a_2}$ and goes beyond the $\frac{v_{dc}}{2}$ in successive sampling instants as pictured in Fig. 27(d). Besides, the BTB CMV reaches below the $\frac{-v_{dc}}{2}$ for the fault in switch $S^m_{a_3}$.Therefore, from the analysis, the BTB CMV is affected by the inner switch OS faults and can be incorporated as the additional fault confirmation variable in the fault detection and localization algorithms.

In addition, the robustness of the proposed method under sensor noises is experimentally verified for the sinusoidal ac currents. To do this, the fault diagnosis variable of i^g_a is analyzed for two different cases. In $case-i$, the phase current is applied to current normalization after passing through the general first-order LPF [31]. The response of i^g_a and detection variable γ_{a12} is availed as depicted in Fig. 28(a). Then, in $case-ii$, the measured phase current is passed to current normalization without the LPF and its responses are pictured in Fig. 28(b). Finally, the comparative response of the detection variable under $case-i$ and $case-ii$ is pictured in Fig. 28(c). From, the responses it can be observed that the fault diagnosis variable under sensor noise slightly differs from the noiseless case. However, it does not produce any false positives to trigger the erroneous indication. Thus, the proposed method is robust against sensor noises. Next, Fig. 28(d) shows the sign of derivative availed at the $step-iv$ of the fault diagnosis scheme for the two cases. From this, it

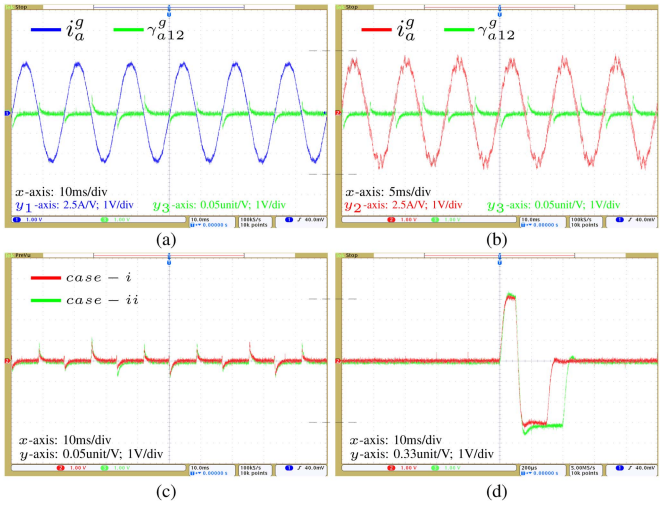

Fig. 28. Robustness of GSC variables against sensor noise. (a) i_a^g and γ_{a12}^g in $case-i$. (b) i_a^g and γ_{a12}^g in $case-ii$. (c) γ_{a12} under $case-i$ and $case-ii$. (d) Derivative responses under $case-i$ and $case-ii$.

can be observed that the sensor noises slightly increase the pulse length thereby slightly increasing the amplitude of the diagnosis variable. However, the change in amplitude is not enough to reach the thresholds. Hence from the response plots, it can be confirmed that the diagnostic variables are within the bounds of thresholds and robust against disturbances and parameter variations.

The conventional method in [21] is based on the derivative of the current's Park's vector. In which, the deformation in vector phase derived from the phase currents is detected by the derivative of the absolute vector phase and employed as the fault detection variable. Then in [22], current form factors are calculated for the measured currents and observed currents. The current form factors are approximately at 1.11 under normal operation and varies accordingly with the various OS fault in the converter, therefore, used as the detection variables. Next, in [29], the zero range duration of phase currents is approximated and used in conjunction with the fundamental period of induced emf and direction of the phase current's previous half cycle to detect and localize the OS fault. Further, in [23], the instantaneous amplitude of the normalized phase currents is estimated as unity for the nondeformed sine wave pattern of currents. Occurrence of OS fault deforms the sine wave pattern of the three phase currents by blocking part of the faulty phase current and distorting the other healthy phase currents. Consequently, the instantaneous amplitude becomes less than unity for the faulty phase and greater than unity for the healthy phase. The phenomenon is employed to evaluate the fault detection variable. Moreover, the evaluated detection variable is utilized to raise the fault flags to indicate the faulty switches. The conventional current normalization in these methods [21], [22], [23], [29] uses the information of dq axes currents from vector control. It introduces errors due to the effect of distorted phase currents in phase-locked loop output, which may affect the robustness and reliability of fault detection system.

Further, unlike conventional methods [21], [22], [23], [29], the proposed method is formulated by analyzing the behavior of current near the zero crossing during the normal operating condition as well as faulty operating conditions. The fluctuation of current near the zero values exhibits unique behavior for each type of OS fault. Therefore, the proposed method is developed based on the behavior of instantaneous current near the zero crossing. In addition to this, the reliability of the method has been improved by introducing the rotor speed-dependent current normalization procedure for 3-level NPC GSC and MSC converters, which specifically applies to the WTS applications. Therefore, the proposed scheme is robust and immune to erroneous fault indication. Moreover, the proposed scheme also utilizes the idea of rising the flags to indicate the faulty switches by using the Algorithms 1 and 2.

Next, to demonstrate the performance of the proposed method, the relevant existing approaches have been compared and summarized for various performance aspects in Table IV. The previously reported current-based methods [21], [22], [23] have moderate computation, and better robustness. Nevertheless, with [21], [22], the localization speed is quite large and the considerable sensitivity to rotor speed variations may cause erroneous fault alarm. In addition, the rotor speed dependency of the fundamental current period leads to inaccurate average current values and affects the performance. Besides, a good trade-off had achieved in [23] with estimated instantaneous current but [22], [23] requires a system model to design the current observer and estimator. Also, all these three methods are tested only with 2 L BTB converters. Hence its applicability to NPC converters is not verified. Furthermore, the zero current duration method in [29] has a low model dependency and fewer computations, but the sensitivity to speed variation is relatively high; also, it does not distinguish the inner and outer-switch faults during UPF operation of GSC. Furthermore, in [24], model-based virtual current mirrors are used with better robustness against parameter variations but tested only with 2 L converters.

Then, the pole voltage-based methods for NPC converters in [19], and [20] are found to be performing better in the detection time. Nevertheless, it requires a higher sampling rate to estimate the pole voltages accurately, thereby increasing the computation. Besides, [19], [20] are tested with constant dc sources. In this case, the capacitor voltage fluctuations due to speed and parameter variations may lead to false estimation of pole voltages and result in erroneous fault alarms. Moreover, in the proposed method, a slightly extended current near the zero value can cause the respective γ to reach the threshold and activate the alarm within a concise duration of less than 30% of the fundamental period. In addition to γ, the δ_c is used as a confirmation variable. Also, the approximation of q-axis current from rotor speed gives an error-free current normalization and further enhances the performance. Therefore, from the above comparison, the proposed method is suitable for BTB NPC converters of high-power-rated PMSG-based WTS. However, the characteristics of power converters differ based on topological structure, and the proposed method cannot be directly adapted to other topologies. Therefore, future research will focus on

TABLE IV
PERFORMANCE COMPARISON OF CONVERTER OS FAULT DIAGNOSIS METHODS

Method	Diagnostic variable	Localization speed	Sensitivity to rotor speed	Complexity	Model dependency	Robustness	Application
[19]	Estimated pole voltage	$< 0.25T$	NA	High	Low	Medium	3L-NPC-VSI
[20]	Quantified pole voltage	Tens of μs	NA	High	Low	Medium	3L-NPC-VSI
[29]	Zero current duration	$< T$	High	Medium	Low	Low	3L-BTB-NPC (WTS)
[21]	Average current	T	Medium	Medium	Low	Medium	2L-BTB (WTS)
[22]	Observed current	T	Medium	Medium	Medium	High	2L-BTB (WTS)
[23]	Instantaneous current	$< 0.5T$	Low	Medium	Medium	High	2L-BTB (WTS)
[24]	Virtual current	$0.7T$ to $1.2T$	NA	Low	High	High	2L-VSI
Proposed	Instantaneous current	$< 0.3T$	Low	Low	Low	High	3L-BTB-NPC (WTS)

developing the adaptive ZRV-based fault diagnosis method for various converter topologies.

V. CONCLUSION

This study has presented an OS fault detection and localization method to enhance the reliability and availability of 3 L BTB NPC converter-fed PMSG-based high-power WTS. To do this, the principle diagnostic variable γ has been formulated for MSC and GSC by defining the ZRV i_{yz} and fault confirmation variable δ_c. Moreover, the ripples near the zero value of phase current under fault occurrence have been effectively used as a ZRV to approximate the γ values. Further, thresholds have been defined to detect and localize the faulty switch; subsequently, Algorithms 1 and 2 have been evaluated for MSC and GSC, respectively. At that time, WTS rotor speed-based q-axis current approximation has been introduced for both MSC and GSC to avoid the effect of distorted phase currents in current normalization. Then, the proposed method has been verified for its effectiveness in OS fault detection. Afterward, the immunity to erroneous indications under highly fluctuating load, parameter variations, and ac/dc side disturbances has been demonstrated by simulation and hardware implementation.

REFERENCES

[1] Z. Zhang, X. Zhao, L. Fu, and M. Edrah, "Stability and dynamic analysis of the PMSG-based WECS with torsional oscillation and power oscillation damping capabilities," *IEEE Trans. Sustain. Energy*, vol. 13, no. 4, pp. 2196–2210, Oct. 2022.

[2] B. Sun, Z. Chen, C. Gao, A. Haddad, J. Liang, and X. Liu, "A power decoupling control for wind power converter based on series-connected MMC and open-winding PMSG," *IEEE Trans. Ind. Electron.*, vol. 69, no. 8, pp. 8091–8101, Aug. 2022.

[3] X. Yuan, "A set of multilevel modular medium-voltage high power converters for 10-MW wind turbines," *IEEE Trans. Sustain. Energy*, vol. 5, no. 2, pp. 524–534, Apr. 2014.

[4] L. G. Franquelo, J. Rodriguez, J. I. Leon, S. Kouro, R. Portillo, and M. A. Prats, "The age of multilevel converters arrives," *IEEE Ind. Electron. Mag.*, vol. 2, no. 2, pp. 28–39, Jun. 2008.

[5] U. Shipurkar, E. Lyrakis, K. Ma, H. Polinder, and J. A. Ferreira, "Lifetime comparison of power semiconductors in three-level converters for 10-MW wind turbine systems," *IEEE Trans. Emerg. Sel. Topics Power Electron.*, vol. 6, no. 3, pp. 1366–1377, Sep. 2018.

[6] K. Ma and F. Blaabjerg, "Modulation methods for neutral-point-clamped wind power converter achieving loss and thermal redistribution under low-voltage ride-through," *IEEE Trans. Ind. Electron.*, vol. 61, no. 2, pp. 835–845, Feb. 2014.

[7] A. Isidori, F. M. Rossi, F. Blaabjerg, and K. Ma, "Thermal loading and reliability of 10-MW multilevel wind power converter at different wind roughness classes," *IEEE Trans. Ind. Appl.*, vol. 50, no. 1, pp. 484–494, Jan./Feb. 2014.

[8] M. Chen and Y. He, "Multiple open-circuit fault diagnosis method in NPC rectifiers using fault injection strategy," *IEEE Trans. Power Electron.*, vol. 37, no. 7, pp. 8554–8571, Jul. 2022.

[9] J. Liang, K. Zhang, A. Al-Durra, and D. Zhou, "A multi-information fusion algorithm to fault diagnosis of power converter in wind power generation systems," *IEEE Trans. Ind. Informat.*, 2023, to be published, doi: 10.1109/TII.2023.3271358.

[10] M. Kamarzarrin, M. H. Refan, and P. Amiri, "Open-circuit faults diagnosis and fault-tolerant control scheme based on sliding-mode observer for DFIG back-to-back converters: Wind turbine applications," *Control Eng. Pract.*, vol. 126, 2022, Art. no. 105235, doi: 10.1016/j.conengprac.2022.105235.

[11] S. K. Rastogi, S. S. Shah, B. N. Singh, and S. Bhattacharya, "Mode analysis, transformer saturation, and fault diagnosis technique for an open-circuit fault in a three-phase DAB converter," *IEEE Trans. Power Electron.*, vol. 38, no. 6, pp. 7644–7660, Jun. 2023, doi: 10.1109/TPEL.2023.3241654.

[12] M. Zhang, Z. Zhang, Z. Li, H. Chen, and D. Zhou, "A unified open-circuit-fault diagnosis method for three-level neutral-point-clamped power converters," *IEEE Trans. Power Electron.*, vol. 38, no. 3, pp. 3834–3846, Mar. 2023, doi: 10.1109/TPEL.2022.3218427.

[13] J. Kucka and D. Dujic, "Shoot-through protection for an IGCT-based ZVS resonant DC transformer," *IEEE Trans. Ind. Electron.*, vol. 70, no. 3, pp. 3209–3212, Mar. 2023, doi: 10.1109/TIE.2022.3170614.

[14] A. V. Rocha, S. Bhattacharya, G. K. Moghaddam, R. D. Gould, H. de Paula, and B. de Jesus Cardoso Filho, "Thermal stress and high-temperature effects on power devices in a fault-resilient NPC IGCT-based converter," *IEEE Trans. Power Electron.*, vol. 31, no. 4, pp. 2800–2807, Apr. 2016, doi: 10.1109/TPEL.2015.2452262.

[15] W. Zhou et al., "Comprehensive analysis and experiment of extreme faults in MMC based on IGCT," *IEEE Trans. Power Electron.*, vol. 38, no. 5, pp. 6272–6282, May 2023, doi: 10.1109/TPEL.2023.3238374.

[16] J. Liang, K. Zhang, A. Al-Durra, S. Muyeen, and D. Zhou, "A state-of-the-art review on wind power converter fault diagnosis," *Energy Rep.*, vol. 8, pp. 5341–5369, 2022.

[17] J. Zhang, X. Hu, S. Xu, Y. Zhang, and Z. Chen, "Fault diagnosis and monitoring of modular multilevel converter with fast response of voltage sensors," *IEEE Trans. Ind. Electron.*, vol. 67, no. 6, pp. 5071–5080, Jun. 2020.

[18] C. Yang et al., "Voltage difference residual-based open-circuit fault diagnosis approach for three-level converters in electric traction systems," *IEEE Trans. Power Electron.*, vol. 35, no. 3, pp. 3012–3028, Mar. 2020.

[19] M. Chen and Y. He, "Open-circuit fault diagnosis method in NPC rectifiers using fault-assumed strategy," *IEEE Trans. Power Electron.*, vol. 37, no. 11, pp. 13668–13683, Nov. 2022.

[20] S. Ahmadi, P. Poure, S. Saadate, and D. A. Khaburi, "A real-time fault diagnosis for neutral-point-clamped inverters based on failure-mode algorithm," *IEEE Trans. Ind. Informat.*, vol. 17, no. 2, pp. 1100–1110, Feb. 2021.

[21] N. M. Freire, J. O. Estima, and A. J. M. Cardoso, "Open-circuit fault diagnosis in PMSG drives for wind turbine applications," *IEEE Trans. Ind. Electron.*, vol. 60, no. 9, pp. 3957–3967, Sep. 2013.

[22] I. Jlassi, J. O. Estima, S. K. El Khil, N. M. Bellaaj, and A. J. M. Cardoso, "Multiple open-circuit faults diagnosis in back-to-back converters of PMSG drives for wind turbine systems," *IEEE Trans. Power Electron.*, vol. 30, no. 5, pp. 2689–2702, May 2015.

[23] S. Xu, S. Tao, W. Zheng, Y. Chai, M. Ma, and L. Ding, "Multiple open-circuit fault diagnosis for back-to-back converter of PMSG wind generation system based on instantaneous amplitude estimation," *IEEE Trans. Instrum. Meas.*, vol. 70, 2021, Art. no. 3512413.

[24] Z. Huang, Z. Wang, and C. Song, "Complementary virtual mirror fault diagnosis method for microgrid inverter," *IEEE Trans. Ind. Informat.*, vol. 17, no. 11, pp. 7279–7290, Nov. 2021.
[25] U. M. Choi, J. S. Lee, F. Blaabjerg, and K. B. Lee, "Open-circuit fault diagnosis and fault-tolerant control for a grid-connected NPC inverter," *IEEE Trans. Power Electron.*, vol. 31, no. 10, pp. 7234–7247, Oct. 2016.
[26] D. Zhou and Y. Tang, "A model predictive control-based open-circuit fault diagnosis and tolerant scheme of three-phase AC–DC rectifiers," *IEEE Trans. Emerg. Sel. Topics Power Electron.*, vol. 7, no. 4, pp. 2158–2169, Dec. 2019.
[27] Z. Li, H. Ma, Z. Bai, Y. Wang, and B. Wang, "Fast transistor open-circuit faults diagnosis in grid-tied three-phase VSIs based on average bridge arm pole-to-pole voltages and error-adaptive thresholds," *IEEE Trans. Power Electron.*, vol. 33, no. 9, pp. 8040–8051, Sep. 2018.
[28] C. Sui, Y. He, Z. Li, and M. Chen, "The post-fault current model of voltage source converter and its application in fault diagnosis," *IEEE Trans. Power Electron.*, vol. 36, no. 2, pp. 1209–1214, Feb. 2021.
[29] J. S. Lee, K. B. Lee, and F. Blaabjerg, "Open-switch fault detection method of a back-to-back converter using NPC topology for wind turbine systems," *IEEE Trans. Ind. Appl.*, vol. 51, no. 1, pp. 325–335, Feb. 2015.
[30] K. Palanimuthu, G. Mayilsamy, S. R. Lee, S. Y. Jung, and Y. H. Joo, "Fault ride-through for PMVG-based wind turbine system using coordinated active and reactive power control strategy," *IEEE Trans. Ind. Electron.*, vol. 70, no. 6, pp. 5797–5807, Jun. 2023.
[31] S. Golestan, M. Ramezani, J. M. Guerrero, F. D. Freijedo, and M. Monfared, "Moving average filter based phase-locked loops: Performance analysis and design guidelines," *IEEE Trans. Power Electron.*, vol. 29, no. 6, pp. 2750–2763, Jun. 2014.
[32] B. Wu, Y. Lang, N. Zargari, and S. Kouro, *Power Conversion and Control of Wind Energy Systems*. Hoboken, NJ, USA: Wiley, 2011.
[33] A. Bakbak, H. T. Canseven, M. Ayaz, M. Altintaş, and E. Meşe, "Maximizing energy extraction from direct grid coupled PMSG for wind energy conversion systems," *IEEE Trans. Ind. Appl.*, vol. 58, no. 3, pp. 3888–3900, May/Jun. 2022.
[34] R. P. Antonysamy, S. R. Lee, S. Y. Jung, and Y. H. Joo, "Performance enhancement using robust sliding mode approach-based current control for PMVG-WECS," *IEEE Trans. Ind. Electron.*, vol. 70, no. 10, pp. 10156–10166, Oct. 2023.
[35] M. Mehendale, S. Sherlekar, and G. Venkatesh, "Low-power realization of FIR filters on programmable DSPs," *IEEE Trans. Very Large Scale Integr. Syst.*, vol. 6, no. 4, pp. 546–553, Dec. 1998, doi: 10.1109/92.736126.
[36] K. Palanimuthu, G. Mayilsamy, S. R. Lee, S. Y. Jung, and Y. H. Joo, "Comparative analysis of maximum power extraction and control methods between PMSG and PMVG-based wind turbine systems," *Int. J. Elect. Power Energy Syst.*, vol. 143, 2022, Art. no. 108475.
[37] G. Mayilsamy, S. R. Lee, and Y. H. Joo, "An improved model predictive control of back-to-back three-level NPC converters with virtual space vectors for high power PMSG-based wind energy conversion systems," *ISA Trans.*, vol. 143, pp. 503–524, 2023, doi: 10.1016/j.isatra.2023.09.033.
[38] K. Xie, Z. Jiang, and W. Li, "Effect of wind speed on wind turbine power converter reliability," *IEEE Trans. Energy Convers.*, vol. 27, no. 1, pp. 96–104, Mar. 2012.
[39] X. Xu, Z. Zheng, K. Wang, B. Yang, and Y. Li, "A comprehensive study of common mode voltage reduction and neutral point potential balance for a back-to-back three-level NPC converter," *IEEE Trans. Power Electron.*, vol. 35, no. 8, pp. 7910–7920, Aug. 2020, doi: 10.1109/TPEL.2019.2961385.
[40] X. Xu, Z. Zheng, K. Wang, B. Yang, and Y. Li, "A carrier-based common-mode voltage elimination method for back-to-back three-level NPC converters," *IEEE Trans. Power Electron.*, vol. 37, no. 3, pp. 3040–3052, Mar. 2022, doi: 10.1109/TPEL.2021.3112697.

Ganesh Mayilsamy received the B.S. degree in electrical and electronics engineering from Sasurie College of Engineering, Vijayamangalam affiliated to Anna University, Tamilnadu, India, in 2008, the M.S. degree in power electronics and drives from ACCET, Karaikudi, India in 2011. He is currently working toward the Ph.D. degree in electrical and electronic control engineering with the School of IT Information and Control Engineering, Kunsan National University, Gunsan, South Korea.

Then, he was an Assistant Professor with the Department of Electrical and Electronics Engineering, P.A. College of Engineering, Pollachi, India. His current research interests include power electronics drives and wind turbine control.

Seong Ryong Lee received the B.Sc. and M.Sc. degrees in electrical engineering from Myong-Ji University, Seoul, South Korea in 1980 and 1982, respectively, and the Ph.D. degree in electrical engineering from Chonbuk National University, Jeonju, South Korea, in 1988.

Since 1990, he is currently a Professor with the School of IT Information and Control Engineering, Kunsan National University, Gunsan, South Korea. And he was a Visiting Professor with the Department of Electrical and Computer Engineering at Virginia Tech., USA, from 1997 to 1998 and, also at the Curtin University of Technology, Perth, Australia from 2004 to 2006. His research interests include power electronics, control, and grid-interactive renewable energy systems.

Young Hoon Joo received the B.S., M.S., and Ph.D. degrees in electrical engineering from Yonsei University, Seoul, South Korea, in 1982, 1984, and 1995, respectively.

He was a Project Manager with Samsung Electronics Company, Seoul, from 1986 to 1995. He was a Visiting Professor with the Department of Electrical and Computer Engineering, University of Houston, Houston, TX, USA, from 1998 to 1999. He is currently a Professor with the School of IT Information and Control Engineering, Kunsan National University, Gunsan, South Korea (1995 current). His research interests include control engineering, nonlinear system, intelligent control, wind energy systems, and computer vision.

Dr. Joo served as the President of the Korea Institute of Intelligent Systems in 2009, the Editor-in-Chief of the International Journal of Control, Automation, and Systems (IJCAS, IF: 3.314) from 2014 to 2017, the Vice-President of the Institute of Control, Robot, and Control from 2016 to 2017, and the President for the Korean Institute of Electrical Engineers in 2019. He is serving as the Director of the Research Center of Wind Energy Systems, at Kunsan National University funded by the Korean Government (2016 current).